UCRL 15892
P.O. 6419309

final report

MASTER

INERTIAL CONFINEMENT FUSION RESEARCH & DEVELOPMENT STUDIES

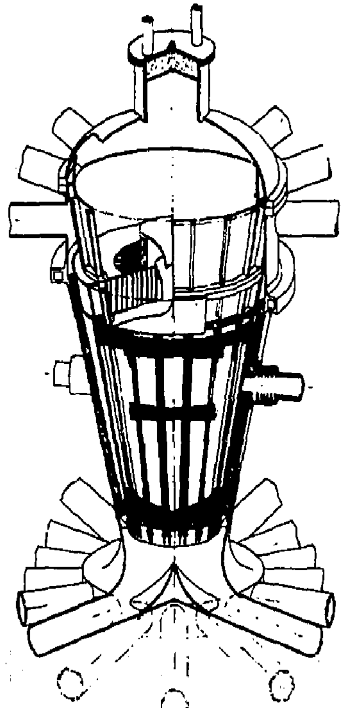

GRUMMAN AEROSPACE CORPORATION

UCRL 15292
P.O. 6419308 Copy No. 6 of 47

final report

INERTIAL CONFINEMENT FUSION RESEARCH & DEVELOPMENT STUDIES

performance period - October 1979 to August 1980

prepared for
University of California
Lawrence Livermore National Laboratory

by
R. Bullis
M. Finkelman
J. Leng
T. Luzzi
I. Ojalvo
E. Powell
D. Sedgley

Grumman Aerospace Corporation
Bethpage, New York 11714

August 1980

FOREWORD

The Lawrence Livermore National Laboratory (LLNL) of Livermore, California contracted the Grumman Aerospace Corporation to provide level-of-effort engineering support services in accordance with Purchase Order 6419309, dated August 1979, Appendix A - Scope of Work, Task 1. This work was performed at the Grumman Aerospace Corporation, Bethpage, New York under the direction of Mr. R. Botwin, Assistant Director of Advanced Energy Systems at Grumman. Dr. J. Pitts was the LLNL technical monitor for this task.

ACKNOWLEDGEMENTS

The authors wish to thank Dr. M. Monsler, Dr. J. Pitts, Mr. J. Hovingh, Dr. L. Glenn, and Mr. J. Blink for their guidance and constructive critique of the work performed.

CONTENTS

CONTENTS (contd)

ILLUSTRATIONS

ILLUSTRATIONS (contd)

ILLUSTRATIONS (contd)

1 - INTRODUCTION & SUMMARY

1.1 INTRODUCTION

The Advanced Energy Systems Group of Grumman Aerospace Corporation provided technical support services to the Lawrence Livermore National Laboratory during the period from Octover 1979 to August 1980. These Inertial Confinement Fusion (ICF) research and development studies were for selected structural, thermal, and vacuum pumping analyses in support of the High Yield Lithium Injection Fusion Energy (HYLIFE) concept development. An additional task provided an outlined program plan for an ICF Engineering Test Facility, using the HYLIFE concept as a model, although the plan is generally applicable to other ICF concepts.

The HYLIFE is one promising type of ICF concept which features a falling array of liquid lithium jets. These jets surround the fusion reaction to protect the first structural wall (FSW) of the vacuum chamber by absorbing the fusion energy, and to act as the tritium breeder (Subsection 1.3, Ref 1-1). The fusion energy source is a deuterium-tritium pellet injected into the chamber every second and driven by laser or heavy ion beams. The studies performed by Grumman have considered the capabilities of specific HYLIFE features to meet life requirements and the requirement to recover to preshot conditions prior to each subsequent shot. The components under investigation were the FSW which restrains the outward motion of the liquid lithium, the nozzle plate which forms the falling jet array, the graphite shield which is in direct top view of the fusion pellet, and the vacuum pumping system. The FSW studies included structural analysis, and definition of an experimental program to validate computer codes describing lithium motion and the resulting impact on the wall.

1.2 SUMMARY

1.2.1 First Structural Wall Structural Analysis

The HYLIFE FSW absorbs pulsating fusion reaction loads so that a low-level steady-state load is felt by the vacuum vessel. An alternate wall design was considered, which consisted of multiple layers of helically wound bars, with each layer spaced and alternately pitched to absorb gradually the radial momentum of the liquid metal array.

The study evaluated only the innermost helical layer which has the highest loading. The forcing function grows in complexity for other layers, and it was believed that the single layer results were adequate and consistent with order-of-magnitude calculations associated with a conceptual design study.

The study showed that most of the impact pressure occurs over a time interval which is very short compared to the natural period of helix motion, which in turn is short compared to the time it takes for one-half meter of fluid to pass over the first row of turns. Thus, damping is unimportant in limiting peak helix stresses. Structural damping over 0.3% is required to permit a 1-Hz firing frequency, and steel materials with this characteristic can be obtained although not readily.

The helix motion damping mechanism is the most crucial item exposed by the study, because structural damping is marginal for high fusion pulse frequencies.

1.2.2 Nozzle Plate Structural Analysis

The nozzle plate creates an array of lithium jets and is designed to support static loads from the lithium head, friction drag, and dead weight of the plate; as well as dynamic loads from neutron-induced pressure above the plate and superheated lithium gas pressure below. The plate design is a weldment of extruded angles simply supported at its outer circumference, with an annular weir at its inner radius to control lithium flow through the plate central orifice. This analytically complex design was idealized as an homogeneous axisymmetric plate with nonuniform orthotropic mass and stiffness properties.

The structural analyses showed that the nozzle plate can be made much thinner than the 140 cm which was evaluated. The design approach would be to select a static stress compatible with the material and with the calculated dynamic stress computed for an appropriate stress concentration factor. The plate thickness could be reduced according to scaling laws defined in the study.

1.2.3 Graphite Plug Thermal Analysis

The graphite top plug protects the portion of the HYLIFE top closure which has a "direct view" of the pellet fusion reaction. An active cooling system to protect the plug from neutron, X-ray, and debris loading was analyzed considering the cooling channels on the plug back surface and the cooling channels buried inside the plug.

The study showed that buried channels were required to maintain temperature profiles inside the plug within an acceptable range, and that coolant flow requirements were not difficult to satisfy.

1.2.4 Vacuum Pumping System Analysis

The vacuum pumping system removes constituents, principally hydrogen isotopes and helium, from the vessel cavity during a portion of the time between fusion shots, so that preshot conditions are restored prior to each subsequent shot. The study analyzed the pumping requirements and defined conceptually the pumping system components.

The study showed that the high pumping capacity which is needed for the high vacuum range requires pumping systems that are too large to be practical; consequently, alternatives to direct pumping of the cavity should be assessed.

1.2.5 Shock Tunnel Blowthrough Experiment Design

A design study was performed to define an experiment for verification of a one-dimensional code describing lithium plasma flow over a liquid jet array. High temperatures and energies coupled with lithium handling could mean a complex, expensive experiment; however, a major portion of the code could be verified simply in the low energy regime over simulated jets.

The simulation developed in the study consisted of a jet array represented by rigid cylindrical posts in the test section of a shock tunnel. The test program would provide time-varying fluid pressure in the test section.

Two test options are presented. In one option, the test initial conditions would be pressure and temperature in the driven tube stagnation region (upstream of the test section). The other option would use initial pressure and temperature (and velocity) conditions, which would be determined experimentally at a test station downstream of the test section threat. Proof of principle experiments for determining velocity by laser Doppler velocimeter and temperature by infrared emission are recommended.

1.2.6 Engineering Test Facility Planning

The Engineering Test Facility (ETF) is a proposed testbed for ICF reactor engineering and technology. This study provides a preliminary assessment of ETF objectives and expected results, and although it uses the HYLIFE concept as a model, the program thus defined could be adapted readily to other driver/energy converter methods. Three areas requiring significant development are: the driver, the pellet target, and the energy converter; with the last activity being addressed currently on a small scale only, compared to the other two. The ETF would demonstrate integration of these three systems.

The study outlines the current state of planning for the ICF ETF, and itemizes the engineering development that must precede it. It is expected that most engineering development testing could be completed during a 5-yr period, after which the ETF could be reconfigured to meet programmatic needs of a materials test or tritium production facility.

1.3 REFERENCE

The following reference has been cited in this section:

1-1 Lawrence Livermore National Laboratory, "Potential Design Modifications for the High Yield Lithium Injection Fusion Energy Reaction Chamber," by J. H. Pitts, J. Hovingh, W. R. Meier, M. J. Monsler, E. G. Powell, and P. E. Walker, UCRL-82895, 1979

2 - STRUCTURAL DYNAMICS

2.1 INTRODUCTION

The HYLIFE reaction chamber (Fig. 2-1) contains a First Structural Wall (FSW) that absorbs pulsating loads generated by the fusion reactions so that only an associated much lower secondary load is imposed on the containment structure (vacuum vessel). The radial momentum imparted to the liquid metal jet array after each fusion reaction is absorbed in this FSW. Ideally, the FSW will last the entire 30-yr lifetime of the reaction chamber, but if not, it can be replaced for a fraction of the cost to replace the vacuum vessel.

A simple FSW design involves welding 50-mm-thick ferritic steel plates to form a cylindrical shell. Dispersed liquid from the jet array is stopped abruptly as it hits this slab-type FSW. The rapid transfer of energy results in high stresses, which depending on final determination of input parameters, could restrict the lifetime of a slab FSW below desirable limits.

Because a FSW having a 30-yr lifetime is desirable, an alternative design was conceived that could possibly improve lifetime characteristics. This alternative FSW design consists of multiple layers of bars wound in a helical fashion. Spaces between the bars result in the radial momentum of the jet array being absorbed more gradually than with a slab-type FSW; hence, conceptual stresses are lower. The multiple layers of the helical bar FSW dissipate fluid kinetic energy by promoting splashing interactions of two-phase flow, as the liquid penetrates the array of bars. The number of layers of helical bars needed to dissipate most of the energy is determined so that the fluid exists with an insignificant radial velocity.

This section outlines the structural analyses which were performed on the alternative helical bar-type FSW. A structural analysis of the nozzle plate, which forms the liquid metal jet array pattern and which must withstand transient loadings after each fusion reaction (Fig. 2-2) was also performed.

The analyses confirmed the conceptual feasibility of these design features and yielded basic information regarding the nozzle plate thickness. Also, the results

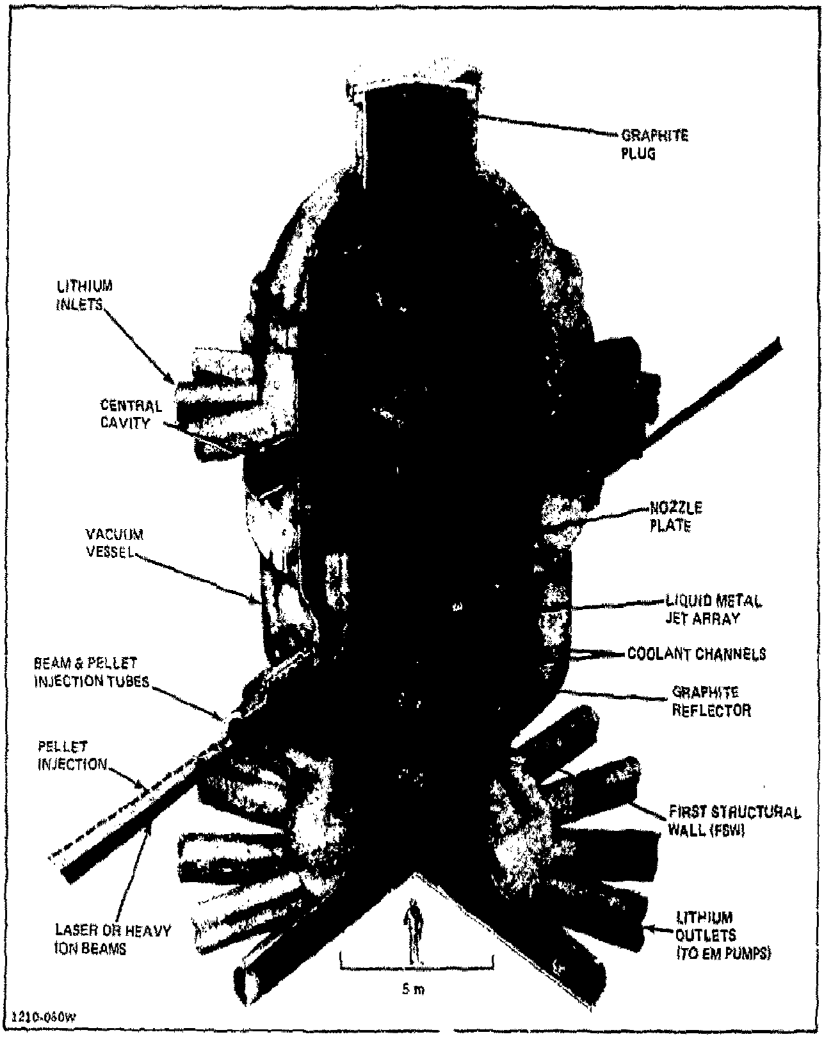

Fig. 2-1 HYLIFE Reactor Chamber

highlighted some questions regarding adequacy of the natural damping mechanisms for the helical energy absorbers.

In general, it should be noted that uncertainties associated with the extreme complexity of the forcing function and the actual structural geometries precluded obtaining detailed structural design information. However, it is felt that these results are adequate and consistent with order-of-magnitude calculations associated with conceptual-design study practices.

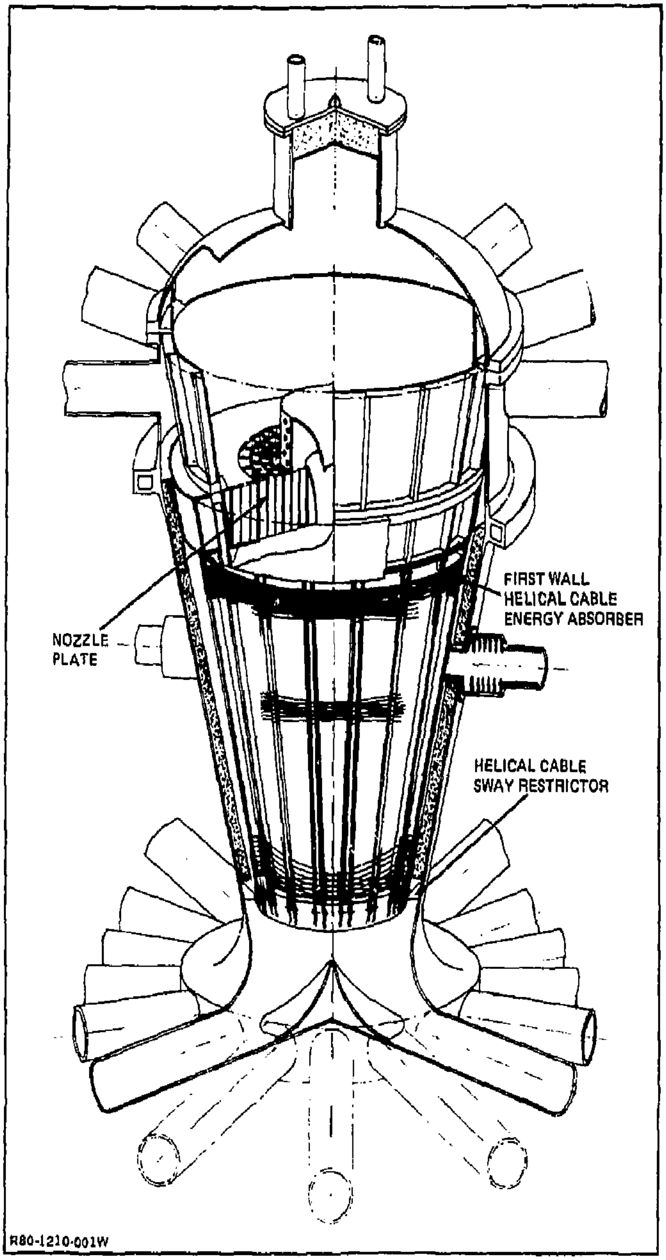

Fig. 2-2 Tapered HYLIFE with Helical Energy Absorbers & Nozzle Plate

2.2 HELICAL BAR FSW

2.2.1 Helical Coil Structural Model

The helical bar FSW is designed as a continuous, 19-mm diameter, 2¼ Cr-1 Mo ferritic steel bar. The inner helical layer is formed by winding the bar material from top to bottom, and the adjacent helical layer is wound from bottom to top to produce a crisscrossing pattern. The winding continues until the desired number of layers is obtained. Center-to-center spacing between the bars in a single layer is 38 mm, which can be adjusted as desired to accommodate fluid dynamic considerations. The helical layers are supported rigidly at the top. A radial sway restrictor is positioned at the bottom to prevent any contact of the bars with either the vacuum vessel or the graphite reflector. The helical layers are held separate from each other by spacers located at discrete positions around the circumference of the FSW.

The FSW deflects vertically under its own weight, and is arranged inside the vacuum vessel so that the lower end reaches the desired position when statically deflected. It deflects elastically a slight amount as liquid lithium impacts the bar layers after each fusion reaction, which helps to absorb the energy of each impact.

Only the innermost helical layer of bars was analyzed because this layer has the highest loading, and because definition of the forcing function grows in complexity for the other helical layers. Figure 2-3 indicates the structural model used to idealize a portion of a turn of the innermost helical layer. Because the pitch is small compared to the radius and the forcing function is axisymmetric, only radial motions were considered. In reality, tangential motions also are possible because the forcing function varies with height, and tangential motions are possible at the top and bottom of the helix. However, these were neglected for the study. Thus, the equations used to model the helix are identical to those for a thin elastic hoop. The dynamic motion of an elastic element is given by the following equation (see Fig. 2-3 for the nomenclature used below):

$$(RPd - T - CR\dot{U}) = m\ddot{U}R \qquad (2\text{-}1)$$

where

R = helix radius

P = applied pressure

d = diameter of helical cable

T = helix tension

C = damping constant for cable of diameter d

U = radial displacement

m = cable mass per unit length

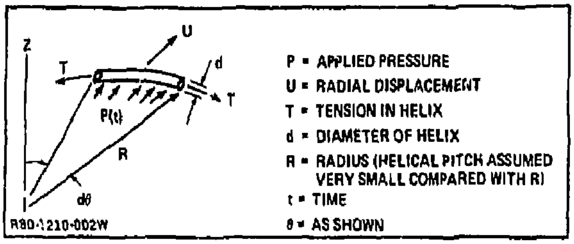

Fig. 2-3 Structural Dynamics for Helical Energy Absorber

The associated cable stress-strain deflection law yields a relationship between cable tension and displacement as follows:

$$T = A\sigma = EA\epsilon = EA\frac{U}{R} \qquad (2\text{-}2)$$

where

A = cable cross sectional area

E = modulus of elasticity

ϵ = strain, U/R

σ = stress, $E \cdot \epsilon$

Therefore, the resulting dynamical equation becomes:

$$m\ddot{U} + C\dot{U} + \frac{EA}{R^2}U = Pd \qquad (2\text{-}3)$$

2.2.2 Forcing Function on Helix

The forcing function used to model the lithium impact upon the helical coil was that of a plane liquid wall of finite width, traveling at a constant velocity (V_F), and striking a solid circular cylinder of diameter d, with axis normal to the fluid velocity. The width chosen for the liquid wall is one-half the sum of the jet widths. This assumption was based partially on the work of Glenn and Young (Subsection 2.4, Ref 2-1), which indicates that the neutron deposition associated with the D-T reaction resulted in a spallation of half the lithium thickness for a solid fall. For multiple jets, which are included in the present design, each jet will split and many of the internal jet splittings will result in net momentum cancellations. It was assumed a liquid width equal to half the sum of the individual jet widths (0.5 m total) would impact the helical coil. However, the peak loading occurs shortly after the initial impact, and would not change appreciably if the total sum of the individual jet widths had been used.

Reference 2-1 presents empirical data for the pressure associated with a finite width wall of fluid impacting a fixed circular cylinder with axis normal to the velocity of the fluid. The initial impact pressure upon the cylinder (P_{max}) has been empirically determined to be given by the relationship:

$$P_{max} = \frac{7}{2} \rho V^2 \qquad (2\text{-}4)$$

where ρ is the fluid mass density, and V is the relative velocity between fluid and cylinder. The associated impact (I_p) imparted to the cylinder is given by:

$$I_p = K_H \frac{\rho \pi V d}{4} \qquad (2\text{-}5)$$

where K_H has been empirically determined to lie somewhere between 0.2 and 0.27. The time (τ) for the fluid to travel around the cylinder defines the impact time. This together with the drag pressure (P_D) after impact are given by the equations

$$\tau = \frac{2I_p}{P_{max}} = \frac{K_H}{7} \frac{\pi d}{V} \qquad (2\text{-}6a)$$

and

$$P_D = C_D \frac{1}{2} \rho V^2 (1 + K_i) \qquad (2\text{-}6b)$$

where K_i is a spacing factor for flow past more than one cylinder (lined up normal to the direction of flow), and is given by:

$$K_i = \frac{0.2d}{S-d}, \quad 0.05 < \frac{S-d}{d} < 2 \qquad (2\text{-}7)$$

where S is the center-to-center spacing of the cylinders. The preceding data are depicted pictorially in Fig. 2-4.

It should be noted that the forcing function of Fig. 2-4 becomes quasi-static when the relative velocity ($V = V_F - \dot{U}$) is used (where V_F is the velocity of the wall of fluid), and that this assumption for V was used in conjunction with the data presented in Ref 2-2.

2.2.3 Helical Bar Vibration Damping

It is anticipated that fusion reactions will occur with a frequency of one per second. Thus it is important to ascertain if there are sufficient mechanisms to virtually dampen the dynamic response prior to initiation of each successive excitation. To investigate the helical damping phenomenon in a preliminary manner, two modes of

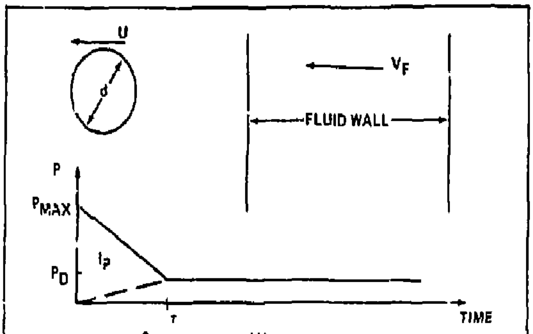

$P_{MAX} = (7/2)\rho V^2, \quad I_P = K_H \frac{\rho\pi d V}{4}, \quad V = V_F - U$

$\tau = K_H \frac{\rho\pi d V}{2P_{MAX}} = (1/7) K_H \frac{\pi d}{V}, \quad P_D = C_D \frac{1}{2} \rho V^2 (1 + K_i)$

K_H = 0.2 TO 0.27

C_D = DRAG COEFFICIENT

K_i = SPACING FACTOR FOR FLOW PAST MORE THAN ONE CYLINDER

R80-1210-003W

Fig. 2-4 Pulse Shape For Fluid Impact on Cylinders

energy dissipation were conceived and a numerical study was performed. The first dissipation mechanism considered was associated with nonlinear fluid viscous damping given by:

$$C\dot{U} \le C_D \frac{1}{2} d\rho \, |\dot{U} - V_F| \, (\dot{U} - V_F) = F_D \qquad (2\text{-}8)$$

and the second was structural damping with

$$C = 2\zeta \sqrt{\frac{mEA}{R^2}} \qquad (2\text{-}9)$$

where ζ is the (assumed) critical damping ratio, F_D is the drag force, and C_D is the drag coefficient for which various values between 0 and 2 were assumed.

2.2.4 Numerical Results

A computer program for numerical solution of the governing equations (Eq 2-2 and 2-3) for purely radial FSW motions was written in FORTRAN and solved on the IBM 370-168 machine. A forward integration scheme, coupled with zero radial displacement and velocity initial-conditions, was used in each case. Typical response results are plotted in Fig. 2-5. The value T_{f_p} on this figure is defined as the time for one-half meter of fluid to pass over the first row of helix turns. As may be seen, most of the impact pressure occurs over a time interval which is very short compared

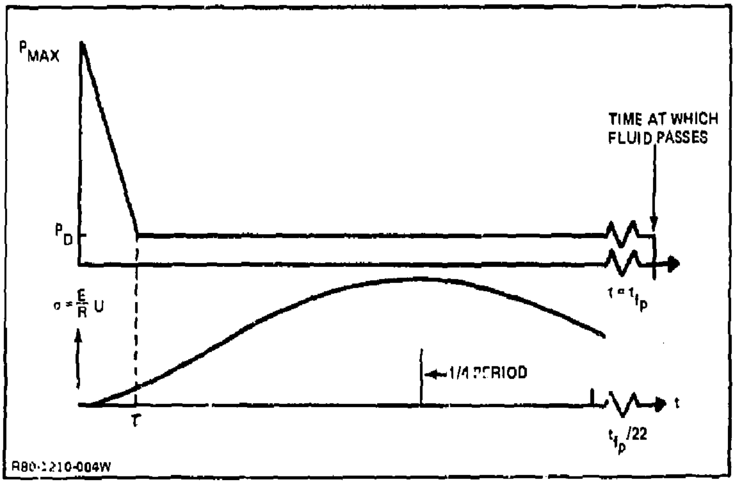

Fig. 2-5 Typical Responses

to the natural period of the helix motion, and that this natural period is short compared to T_{f_p}. Thus, damping is not an important factor in limiting peak FSW helix stresses. Various values for C_D between 0 and 2 were tried, but the results for σ_{max} remained essentially fixed. Furthermore, it was determined that fluid damping alone was hardly capable of attenuating the helix motion between successive pellet firings. Figure 2-6 indicates the dependence of σ_{max} upon V_F.

The effect of structural damping upon helical motion decay is displayed in Fig. 2-7. As may be observed, a minimum of 0.3% is required to permit pellet firings of one per second without significant FSW motion buildup over successive fusion pulses. Reference 2-3 indicates that locating steel materials with such natural damping ability is difficult, but possible. Figure 2-8 shows a typical plot of stress with time for V_F equals 20 m/s.

It should be noted that increasing the helix radius (R) will decrease the peak stresses. The reasoning behind this statement is as follows: The dynamic stresses, which are proportional to dynamic radial motions ($U_{dynamic}$), are produced by impact loading conditions and, therefore, are directly proportional to $\omega^2 U_{static}/R$; where ω is the natural frequency of the motions $U_{dynamic}$, and U_{static} are the static deflections associated with the peak FSW pressures if they were statically applied. For the governing FSW helix structural equations, $\omega^2 \sim 1/R^2$, and $U_{static} \sim R^2 P_{max}$. Thus, $\sigma_{dynamic}$ equals $(EU_{dynamic}/R) \sim P_{max}/R$. In Ref 2-4, Glenn has shown that P_{max} decreases rapidly with increasing R. Hence, a minimum suitable radius can be chosen such that stresses in the helix may be maintained within acceptable limits.

$F_D = (1/2)\, d\, C_D \rho \,|V_F - \dot{U}|\,(V_F - \dot{U})$

FOR: $C_D = 0$ TO 2; $R = 3.3$ m; $d = 2$ cm; $E = 2 \times 10^{11}$ Pa $(30 \times 10^{6}$ psi)

V_F, m/s	P_{MAX}, 10^5 Pa (PSI)	τ, ms	T_{fp}, ms	σ_{MAX}, 10^7 Pa (PSI)
10	1.7 (25)	0.26	52	1.24 (1,800)
20	6.8 (98)	0.13	26	4.1 (5,900)
40	27(394)	0.065	13	14.5 (21,000)

R80-1210-005W

V_F m/s	ζ^*	σ_{MAX}, 10^7 Pa (PSI)	TIME FOR t_{PEAK} TO DROP TO 1% OF σMAX, SECONDS
10	0	1.213 (1759)	∞
	0.001	1.211 (1757)	2.956
	0.003	1.207 (1751)	0.985
	0.010	1.193 (1731)	0.296
20	0.001	3.909 (5669)	2.956
	0.003	3.896 (5651)	0.985
	0.010	3.853 (5589)	0.296
40	0.001	14.08 (20,425)	2.956
	0.003	14.04 (20,364)	0.985
	0.010	13.90 (20,153)	0.296

$\zeta^* = C/C_c$; $P' = P\left[\dfrac{V_F - \dot{U}}{V_F}\right]^2$; $R = 3.3$m; $d = 2$ cm; & $E = 2 \times 10^{11}$ Pa $(30 \times 10^{6}$ PSI)

R80-1210-006W

Fig. 2-7 Cable Dynamic Stresses for Modified Forcing Function (P′) & Structural Damping (ζ)

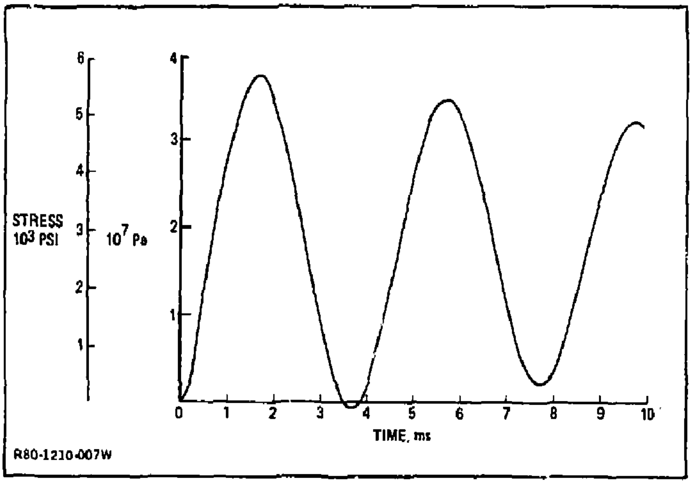

Fig. 2-8 Stress Versus Time For Helical Cable

2.2.5 Helical Coil Preliminary Manufacturing Considerations

The FSW helical coil design was reviewed to determine its manufacturing feasibility within present industrial capability. Forming of the helical coils would probably take place at the reactor site, with special tooling designed to insure pitch consistency. The required handling, bending, and welding equipment would not be excessive, nor should there by any problem in obtaining it. The lengths of each coil segment before welding would be determined by the available lengths of steel bars. In general, the helical coils would be well suited for industrial fabrication.

Weld inspection may present some problems due to accessibility and the confined location of the coils in the vacuum vessel. Thus, the standard verification techniques may not be possible, and new inspection methods may have to be investigated. More detailed fabrication studies would be required to expose possible manufacturing problem areas, and to establish relative manufacturing costs.

2.2.6 Conclusions & Recommendations

Structural dynamics studies on the helical-coil-type First Structural Wall (FSW) for the HYLIFE reaction chamber show that the maximum impact stress varies roughly with the inverse of the wall radius squared, and virtually is independent of the amount of damping present. Because of the rapid decrease of peak stress with increased radius, the wall radius can be selected to maintain the stress within acceptable limits for a given impact velocity. For example, the allowable fatigue limit under HYLIFE operating conditions of 60 MPa for 2¼ Cr-1 Mo ferritic steel is reached with an impact velocity of 25 m/s and the wall placed at a radius of 3.3 m.

Selection of a fusion pulse frequency requires consideration of FSW damping. The study shows the effect of structural damping on the time to recover to a low stress value. Structural damping of about 0.3% will provide recovery within the 1-Hz pulse rate. Steel materials with this damping characteristic can be found, although not readily. If higher pulse frequencies are mandated, the FSW design probably will be more elaborate than that evaluated here. Additional investigation is desirable to assure that adequate damping can be obtained under HYLIFE operating conditions.

2.3 NOZZLE PLATE

2.3.1 Introduction

A nozzle plate is used in the current HYLIFE design (Fig. 2-2) to create a series of lithium vertical jets which absorb the fusion energy. The advantage of jets over a solid annulus or several separate concentric annular rings is that high pressure gases, generated by the energy deposition during fusion reactions, can vent through the interstices between the jets. It is felt that this produces less outward-directed momentum to the FSW. The plate itself must have sufficient strength to support both static and dynamic loads associated with its function and location in the reaction chamber. The nozzle plate static loads arise from the supported lithium head, the friction drag, and the dead weight of the plate. The dynamic loads result from the neutron-induced pressure above the plate and the superheated lithium gas pressure below.

Ability to manufacture and strength were considerations, in addition to function in design of the nozzle plate. The plate design consists of 32-mm-thick extruded angle plates welded together. The nozzle plate is simply supported from the inner liner by a series of gussets. An annular weir flow over the inner radius of the nozzle plate serves to shield the structure from damaging radiation. The plate material is a low-alloy, 2¼ Cr-1 Mo ferritic steel that is compatible with lithium, resistant to hydrogen embrittlement, and produces few radioisotopes.

The following subsections describe the selected nozzle plate structural model, forcing functions, solution procedure, numerical results, scaling laws for similarly loaded different size plates, and manufacturing feasibility; and define additional structural work that should be performed.

2.3.2 Structural Model

Figure 2-2 shows a perspective of the nozzle plate, and a detailed top view of a wedge of the plate is presented in Fig. 2-9. The plate structure is a thick annular plate with nonhomogeneous, nonisotropic properties which are nonuniform in the radial direction. Because of these complexities, and the preliminary nature of this study, the structural model selected to idealize it was a homogeneous axisymmetric plate with nonuniform orthotropic mass and stiffness properties.

The HEX (Ref 2-5) three-dimensional element of the PLANS (Ref 2-6) finite element computer program was used to model the 6-deg plate wedge shown in Fig 2-10. Orthotropic properties, which vary with radius, were used for the 50 eight-noded, six-sided, isoparametric elements. The orthotropic moduli ratios for the annuli used to model the plate also are presented in Fig. 2-10. These properties were based upon local material thickness ratios in the various element directions. The model used assumed that the first two and the last two annuli were closed off with a top plate, which prevented lithium flow and increased the local mass. The inner six annuli did not

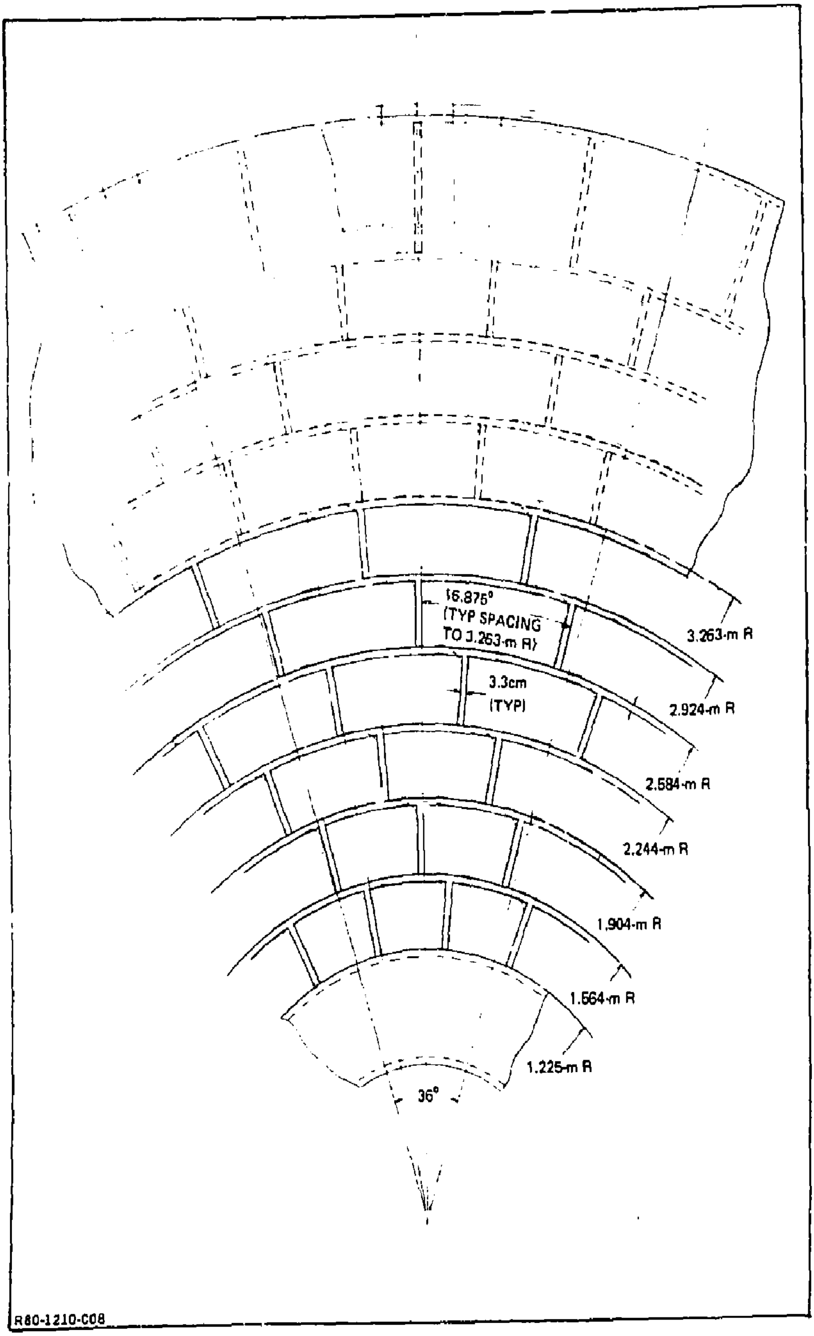

Fig. 2-9 Nozzle Plate Wedge - Top View

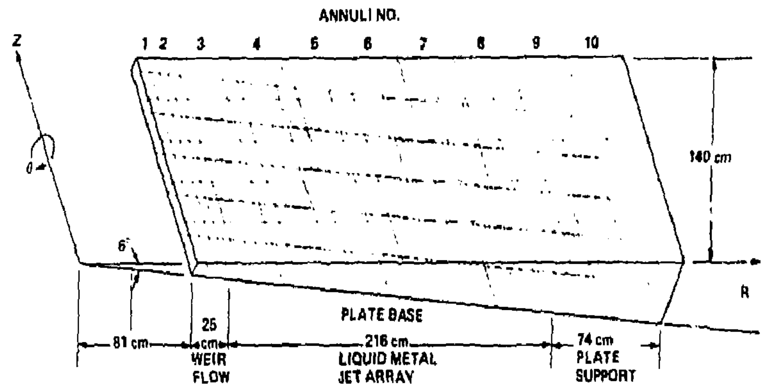

STIFFNESS RATIOS	ANNULI NO.									
	1	2	3	4	5	6	7	8	9	10
E_R/E_{STEEL}	0.036	0.033	0.081	0.066	0.054	0.046	0.041	0.036	0.048	0.043
E_θ/E_{STEEL}	0.097	0.097	0.097	0.097	0.097	0.097	0.097	0.097	0.097	0.097
E_Z/E_{STEEL}	0.132	0.130	0.178	0.162	0.151	0.143	0.138	0.133	0.145	0.140

R80-1210-009W

Fig. 2-10 Nozzle Plate Finite Element Model

permit flow. Axisymmetric boundary conditions on either side of the wedges were used to eliminate circumferential motions.

2.3.3 Forcing Functions

The static load distribution on the nozzle plate is shown in Fig. 2-11. The dead weight of the plate was combined with the lithium weight and applied at the plate top surface purely for convenience. The higher loading at the inner radii was due to the local weir-type structure which prevented fluid from falling on the D-T pellet prior to firing. Friction drag associated with the lithium flow through the nozzles was in the central region of the plate. The extra lithium supported at the outer radius on the steel plate (0.6-cm thick) also was included in the static loading condition.

The plate dynamic downward load, caused by neutron deposition on the upper lithium pool, is presented in Fig. 2-12, while the upward pressure associated with gas pressure in the chamber is presented in Fig. 2-13. These data were supplied by LLNL (Ref 2-3). The dynamic pressure versus time for different values of plate radius (Fig. 2-13) was cross-plotted and is approximated in Fig. 2-14.

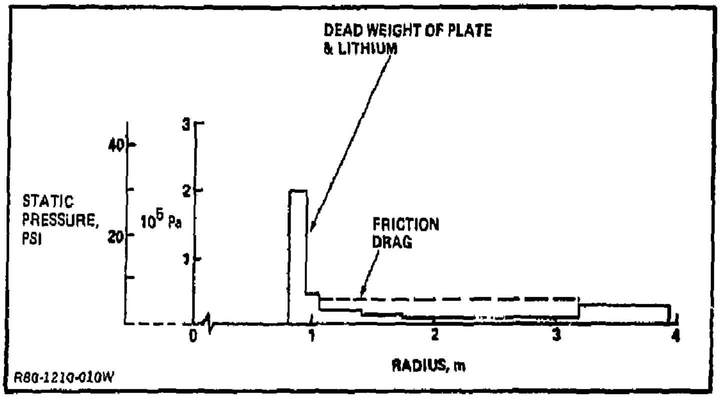

Fig. 2-11 Static Loading on Nozzle Plate Model

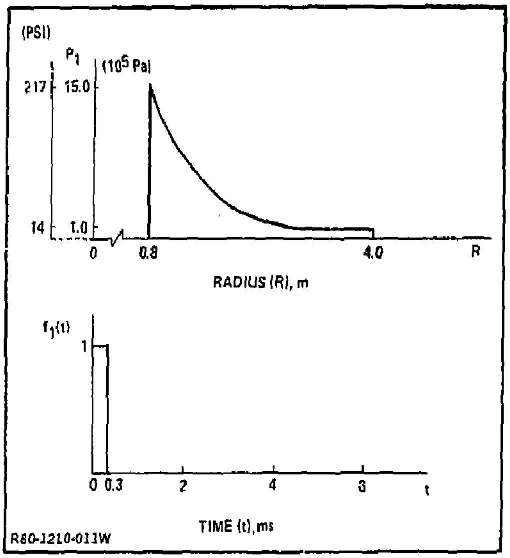

Fig. 2-12 Neutron Energy-Induced Pressure on Top of Nozzle Plate

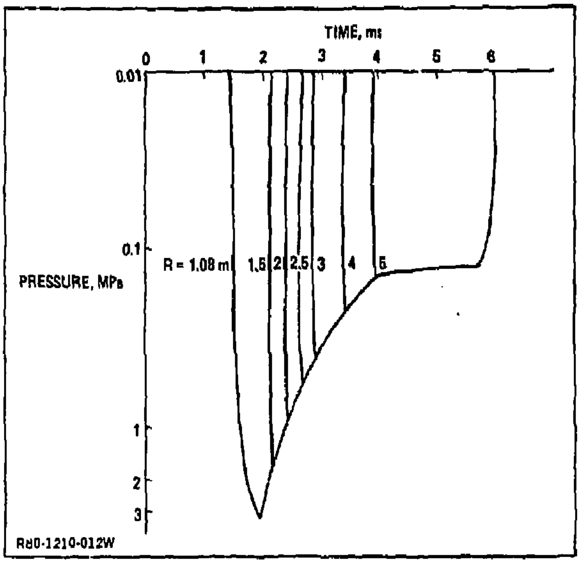

Fig. 2-13 Superheated Gas Upward Pressure Loads on Nozzle Plate

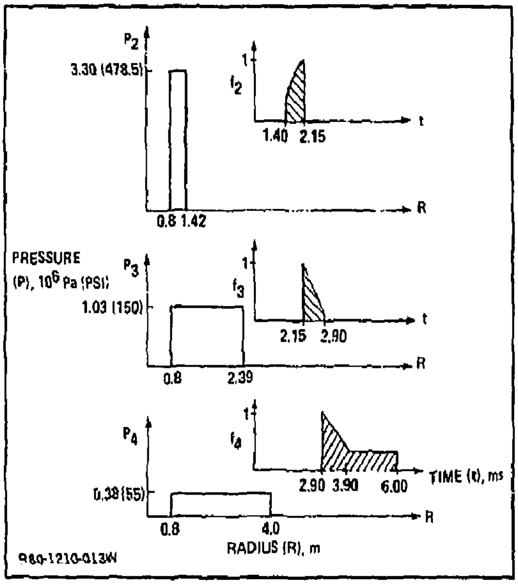

Fig. 2-14 Superheated Lithium Approximate Pressure on Nozzle Plate Bottom

2.3.4 Solution Procedure

A full blown standard dynamic solution by either normal mode or transient response methods was circumvented by using an approximate model approach. The method starts with the governing finite element plate dynamical equations

$$[M]\{\ddot{\delta}\} + [K]\{\delta\} = \{F(t)\} \qquad (2\text{-}10)$$

where [M] and [K] are the plate mass and stiffness matrices, respectively, $\{\delta\}$ are the time-dependent nodal displacements, and {F} are the transient nodal forces. The mass and stiffness matrices are generated by a standard finite element computer program once the appropriate geometry and material properties are inserted as input.

The adopted solution procedure is as follows. The forcing function {F} may be decomposed into a series of products of spatial, $\{P_i\}$, and temporal, $f_i(t)$, functions

$$\{F\} \sim \sum_i \{P_i\} f_i(t) \qquad (2\text{-}11)$$

Approximate solutions of the form

$$\{\delta\} \sim \sum_i \{\delta_i\} X_i(t) \qquad (2\text{-}12)$$

are sought where $\{\delta_i\}$ are assumed modes which satisfy the statical equations, i.e.

$$[K]\{\delta_i\} = \{P_i\}, \quad i=1, 2, \ldots \qquad (2\text{-}13)$$

The use of statical solutions assumes that the dynamic stresses and deflections may be formed as a linear combination of these distributions, where the dynamic stresses, $\{\sigma(t)\}$, are given by the stress matrix, [S], i.e.

$$\{\sigma(t)\} = \sum\{\sigma_i\} = [S]\sum\{\delta_i\}X_i(t) \qquad (2\text{-}14)$$

Substitution of Eq 2-11 through 2-13 into Eq 2-10, and equating in terms of i yields

$$[M]\{\ddot{\delta}_i\} + [K]\{\delta_i\} \sim \{P_i\} f_i = [K]\{\delta_i\} f_i, \quad i=1, 2, \ldots \qquad (2\text{-}15)$$

Multiplying Eq 2-15 by $\{\delta_i\}^T$ and defining ω_{Ri}^2 as the Rayleigh quotient gives the transpose of the nodal displacement vector:

$$\omega_{Ri}^2 = \frac{\{\delta_i\}^T [K] \{\delta_i\}}{\{\delta_i\}^T [M] \{\delta_i\}} = \frac{\{P\}^T \{\delta_i\}}{\{\delta_i\}^T [M] \{\delta_i\}}, \quad i=1, 2, \ldots \qquad (2\text{-}16)$$

and dividing Eq 2-15 by $\{\delta_i\}^T[M]\{\delta_i\}$ yields

$$\ddot{X}_i + \omega_{Ri}^2 X_i = \omega_{Ri}^2 f_i(t), \quad i=1, 2, \ldots \qquad (2\text{-}17)$$

Starting with the forcing functions shown in Fig. 2-12 and 2-14, statical mode shapes $\{\delta_i\}$ and Rayleigh quotients ω_{Ri}^2 were obtained through solution of Eq 2-13 and 2-16, respectively. Then Eq 2-17 was solved by a computerized numerical integration scheme subject to the quiescent initial conditions

$$X_i(0) = 0 \tag{2-18a}$$

$$\dot{X}_i(0) = 0 \tag{2-18b}$$

and the results were combined as indicated by Eq 2-3 to yield an approximation for $\{\delta(t)\}$ and the stresses.

2.3.5 Numerical Results

A peak static stress of 5.2 MPa (750 psi) was obtained for the 3.96-m (156-in.) radius, 1.4-m (55-in.) thick annular nozzle plate subjected to the pressure distribution shown in Fig. 2-11. The peak dynamic stress for the loading of Fig. 2-12 and 2-14 was 16.5 MPa (2400 psi). Both peaks occurred at the same location on the nozzle plate (i.e., at the inner radius of the plate, near the top and bottom surface), and were circumferential components of stress. Typical spatial stress distributions are given in Fig. 2-15 through 2-17. Although these distributions are for a uniform pressure distribution, all the loadings used gave similarly distributed stresses. In fact, all the trial modes yielded Rayleigh quotient frequencies of around 60 Hz. The

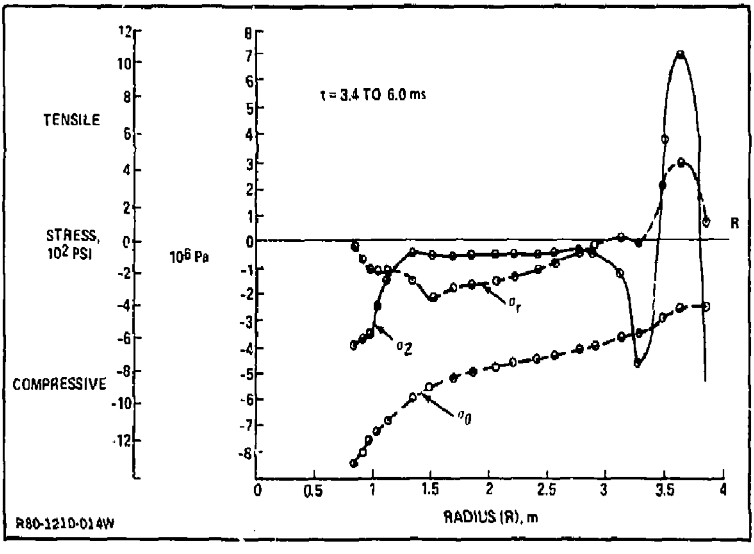

Fig. 2-15 Static Stresses Near Bottom Surface

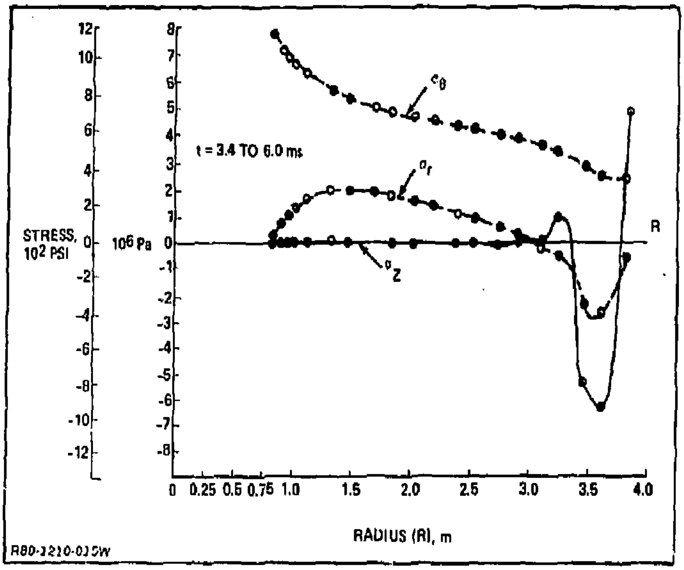

Fig. 2-16 Static Stresses Near Top Surface

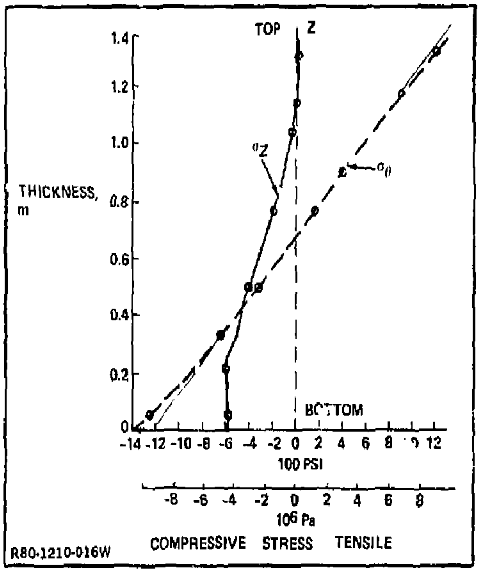

Fig. 2-17 Static Stresses Near Inner Surface

resulting peak stress versus time is shown in Fig. 2-18. This stress includes the effect of nonhomogeneous reduced area in the plate, but does not include local stress concentration effects.

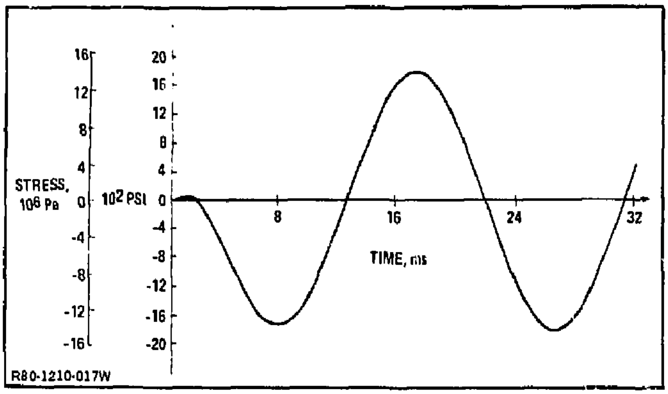

Fig. 2-18 Dynamic Stress Versus Time for Nozzle Plate, Inner Radius Top & Bottom Surfaces

2.3.6 Stress Scaling Laws

Because basic parameters of the present nozzle plate configuration will change as the conceptual design develops, it would be convenient to identify the influence that such changes would have upon primary stresses. As may be seen from Eq 2-12, 2-13, and 2-17, the dynamic plate stresses (σ_d) are proportional to the Rayleigh quotient ω_R^2, and the modal stresses, (σ_a) associated with the "assumed" trial mode shape, i.e.

$$\sigma_d \sim \omega_R^2 \sigma_a \tag{2-19}$$

where

$$\sigma_a \sim q_{dynamic} \left(\frac{a}{h}\right)^2 \tag{2-20}$$

In Eq 2-20, $q_{dynamic}$ is a measurement of the dynamic loading intensity, h is the plate thickness, and a is the plate outer radius.

For a given plate design

$$\omega_R^2 \sim \frac{Eh^2}{\rho a^4} \tag{2-21}$$

where E is the effective plate material stiffness modulus, and ρ is the approximate mass density.

The static stresses (σ_s) however, depend primarily upon the loading parameter (q_s) and the geometric parameters a and h as follows:

$$\sigma_S \sim q_S \left(\frac{a}{h}\right)^2 \tag{2-22}$$

Therefore, increasing the outer plate radius from a to a' will have the effect of increasing the static stresses in the ratio of $(a'/a)^2$, while decreasing the Rayleigh quotient in the ratio $(a/a')^4$. This reduction in $\omega_R{}^2$ would result in a decrease in σ_d by $(a/a')^2$, since σ_a (see Eq 2-20) will increase in the ratio $(a'/a)^2$.

Similarly, an increase in h to h' will cause σ_a and σ_s to go down in the ratio $(h'/h)^2$. However, it will cause σ_d to remain unchanged since the decrease in σ is off-set by a corresponding increase in $\omega_R{}^2$. It should be noted that if the increase in h to h' increases q_{static}, this should be accounted for as well when computing σ_s.

2.3.7 Preliminary Manufacturing Considerations

The nozzle plate design was reviewed to determine its manufacturing feasibility given the present industrial technical capability in this area. It is believed that the angle plates can be welded to form the desired configuration. The fabrication of the nozzle plate would begin with the forming of the walls of the central cylinder. This would be welded to the upper and lower inner cover plates. Next, the angle plates, which compose most of the nozzle plate, are inserted between the upper and lower plates and welded, layer by layer, until the required diameter is obtained.

Construction of the central weir is feasible by most large steel manufacturers (such as Lukins Steel in Coatsville, Pa.). The parts of this assembly would be fabricated in sections and then welded into the final form.

Thus the entire nozzle plate appears to be a straight-forward configuration for industrial manufacturing. However, because of the geometry, it may be difficult to use standard weld verification techniques, and weld inspection techniques may have to be explored.

2.3.8 Conclusions & Recommendations

Based upon the analyses, it appears that the nozzle plate can be made much thinner than the 140-cm configuration which was analyzed. The recommended design approach is to select a static stress which is compatible with the material and with the 16.5-MPa (2400-psi) dynamic stress, computed for an appropriate stress concentration factor (based upon either detailed analysis or fatigue test of the nozzle plate web geometry). The plate thickness then could be reduced according to the scaling laws cited in Subsection 2.3.6 to obtain the desired static stress. In doing this, the static loading should be computed as a function of the plate thickness and weight of lithium required to maintain a static head of 1.2×10^4Pa (102 in.). This static head consideration is based upon maintaining a desired nozzle exit velocity of 5.5 m/s for the lithium fall.

In conclusion, it appears that the proposed nozzle plate configuration represents a viable approach for achieving the desired operational objectives, considering both manufacturing and engineering design viewpoints.

2.4 REFERENCES

The following references have been cited in this section:

2-1 Glen, L. A., and Young, D. A., "Dynamic Loading of the Structural Wall in a Lithium-Fall Fusion Reactor", Nuclear Engineering and Design, 54, 1979, pp 1-16.

2-2 Grumman Aerospace Corporation, Private Communication with R. Kosson, October 18, 1979

2-3 Army Foreign Science and Technology Center, "Vibration Absorbing Properties of Structural Materials; A Handbook," by G. S. Pisarenko, et al, AD-784925, April 1974

2-4 Lawrence Livermore National Laboratory, "On The Motion Following Isochoric Heating of Concentric Liquid Annuli," by L. A. Glenn, UCRL-84003, February 1980

2-5 Grumman Aerospace Corporation, "A Three-Dimensional Variable Node Isoparametric Solid Element," by A. Levy, RM-587, July 1974

2-6 Grumman Aerospace Corporation, "PLANS - A Finite Element Program for the Nonlinear Analysis of Structures," by A. Pifko, et al, RM-633, May 1977

2-7 Lawrence Livermore National Laboratory, Private Communication with J. Blink, January 22, 1980

3 - TOP GRAPHITE PLUG THERMAL ANALYSIS

Preliminary steady-state thermal analyses were performed for the top graphite plug of the HYLIFE Fusion Chamber using a 3.75-m-diameter by 0.88-m-thick plug model that was developed from preliminary drawings. Transient effects from the pulsed nature of the fusion reactions were not included, and may need to be examined in a future study.

For this preliminary analysis, the following thermal loads on the top graphite plug were assumed:

- Neutrons - 0.5 MW/m^3
- X-rays and Debris - 0.3 MW/m^2

The heat generated in the plug due to the neutron load was assumed to be uniformly distributed in space and time, and totaled 4.86 MW. An active cooling system for the plug must be sized for this load as well as the X-ray and debris load. An initial worst case analysis assumed the neutron load uniformly distributed over the area of the plug, so that the total thermal load was equal to a flux of 0.44 MW/m^2. The neutron load was conducted through the plug to the coolant channel at the plug rear face over an assumed average path length of one-half the plug thickness (0.44 m). Using a one-dimensional analysis, temperature differences were calculated for a range of values for the graphite thermal conductivity. Typically, for a representative thermal conductivity of 0.87 W·cm/cm^2K, the temperature difference was 2238 °C.

A similar type of analysis was performed for the X-ray and debris load on the plug surface. The thermal load of 0.3 MW/m^2 was conducted through the thickness of the plug (0.88 m) as an average path length to the coolant channel. For the same typical thermal conductivity of 0.87 W·cm/cm^2K, the temperature difference was 3052 °C.

The temperature differences from neutron, X-ray, and debris loads were added and plotted as a function of graphite thermal conductivity (Fig. 3-1) which included a maximum allowable temperature difference of 3100 °C (based on maximum graphite temperature of 3600 °C and a coolant temperature of 500 °C). While there could be disagreement over some aspects of the analysis (e.g., selected average path length to coolant for neutron load), changes in these parameters would not cause the temperature difference to decrease significantly nor bring them within an acceptable range.

Parametric analyses were added to demonstrate the sensitivity of the results to variations in thermal load. Figure 3-1 also contains plots for ±20% variation in total thermal load (neutrons, X-ray, and debris). The effect on graphite temperature difference is small.

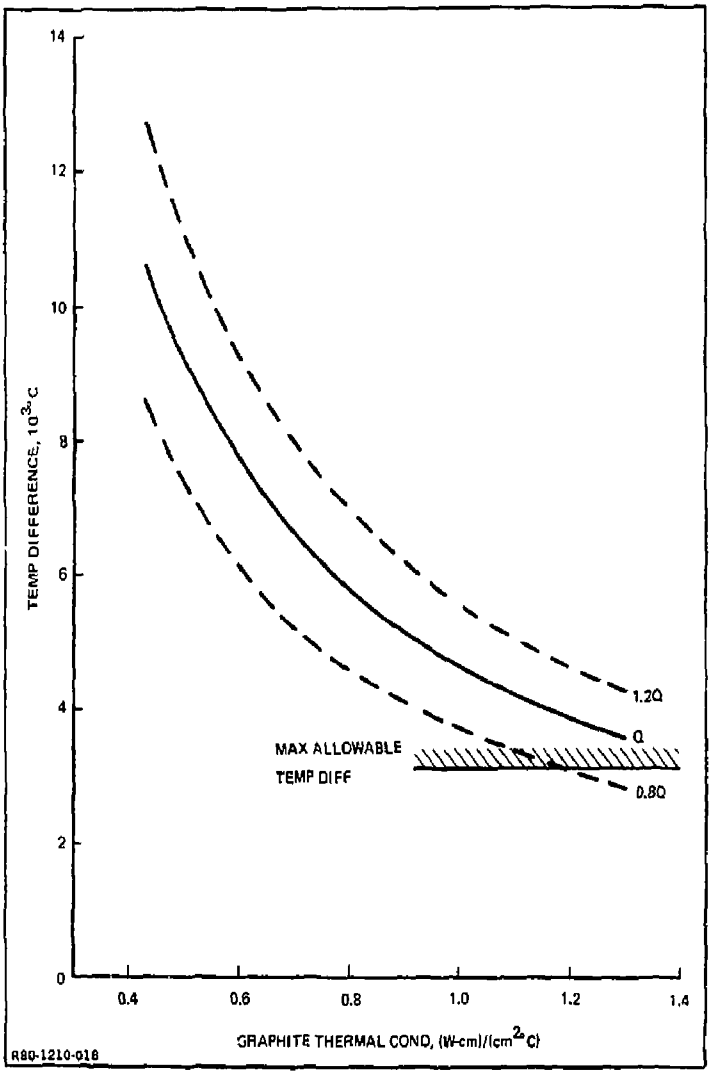

Fig. 3-1 Graphite Top Plug Thermal Response - Cooling Channel at Rear Face

To reduce the temperature differences to an acceptable range, an approach was evaluated in which the coolant channels were internal to the graphite. In particular, a coolant channel spacing of 0.2 m from the hot surface and between each row of channels resulted in the temperature differences plotted in Fig. 3-2. For the range of graphite thermal conductivities considered and for a ±20% in total thermal load, the temperature differences are within an acceptable range. It seems apparent that the graphite top plug must be designed with integral cooling channels.

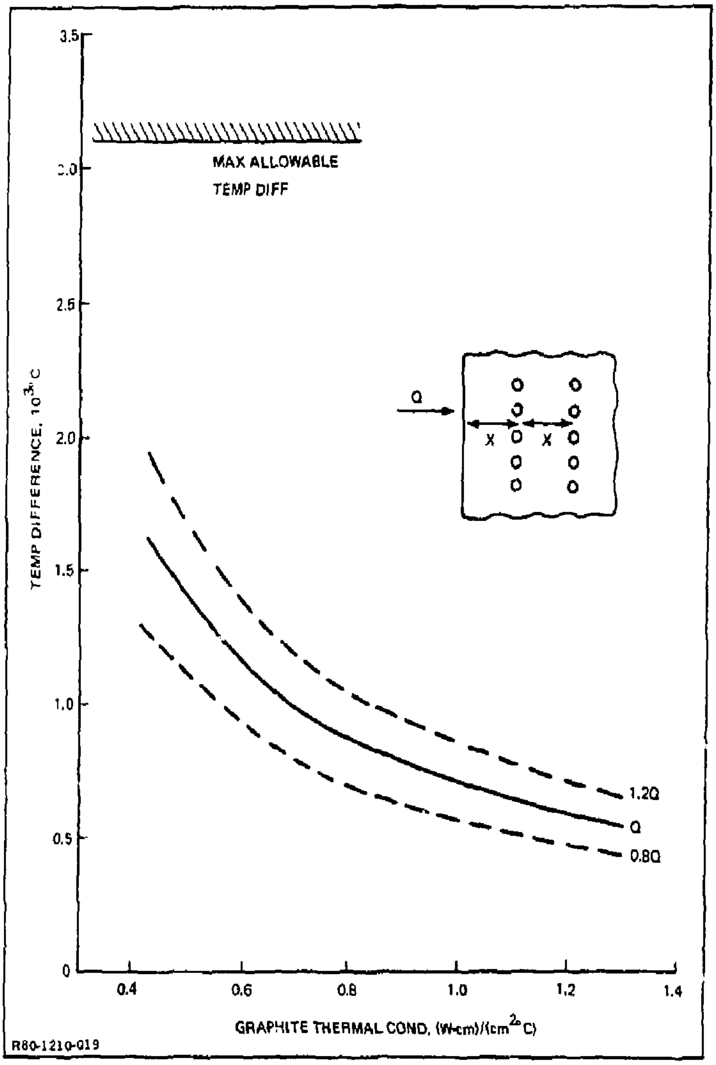

Fig. 3-2 Graphite Top Plug Thermal Response - Cooling Channel at X = 0.2-m Spacing through Graphite

The effect of cooling channel spacing is shown in Fig. 3-3 for a typical graphite thermal conductivity of 0.87 $W \cdot cm/cm^2K$ and a ±20% variation in total thermal load. From these results, it would seem that cooling channel spacing of up to 0.5 m might be acceptable.

Based on the results of these preliminary analyses, it appears that the thermal design of the top graphite plug depends on the integral cooling system design. Con-

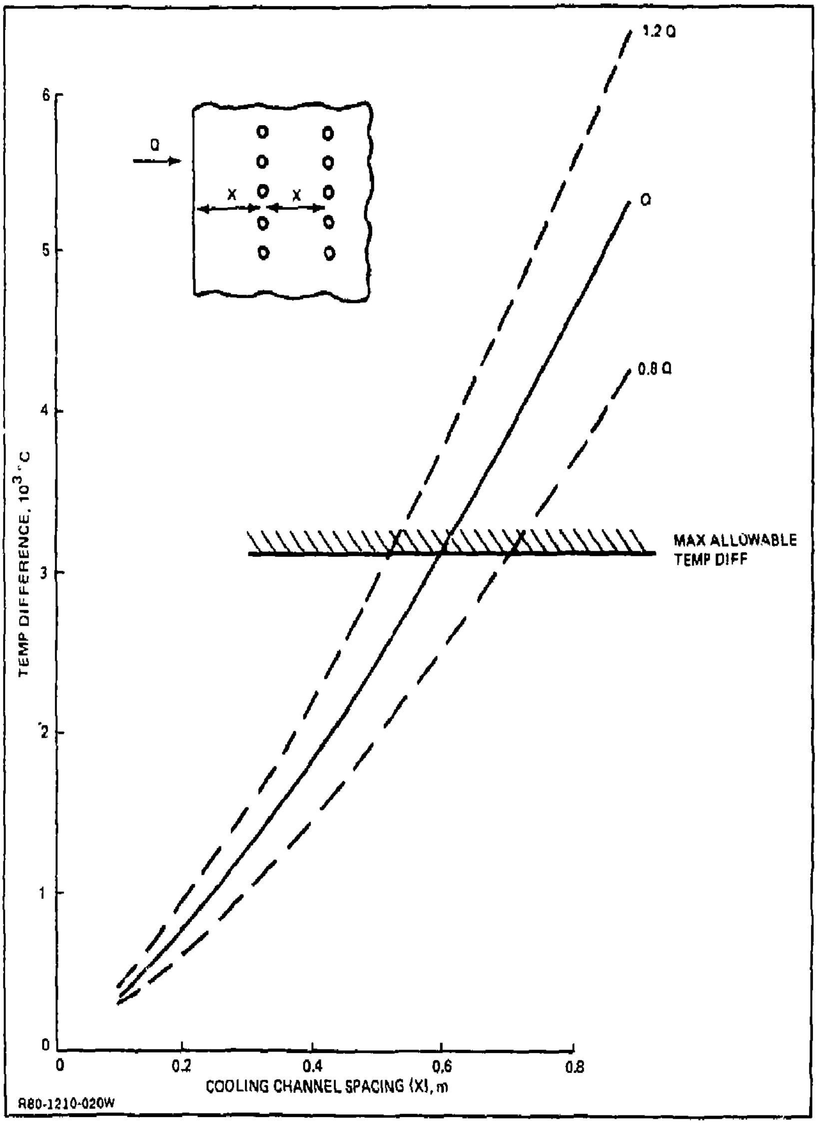

Fig. 3-3 Graphite Top Plug Thermal Response – Thermal Conductivity = 0.87 $(W \cdot cm)/(cm^2 K)$

sequently, no effort was made to perform more detailed two- or three-dimensional thermal analyses for the plug, which would include the effect of heat load distribution within the plug and transient effects.

Estimates also were made of the lithium requirements to actively cool the graphite plug. For lithium at 500 °C and an assumed lithium temperature increase of 5 °C, a total of 0.8 m^3/s is required to handle the total thermal load from neutrons, X-ray, and debris.

4 - VACUUM PUMPING CONSIDERATIONS

4.1 SUMMARY

This section describes a preliminary analysis of the vacuum pumping requirements for the HYLIFE inertial confinement fusion reactor concept. The pumping system removes constituents, principally hydrogen isotopes and helium, from the vessel cavity during a portion of the time between fusion shots, so that preshot conditions are restored prior to the subsequent shot. The conceptual nature of the HYLIFE design means that certain parameters are open. Of particular interest to selection of a pumping system are yield of constituents, pulse frequency, selected liquid metal, and required preshot cavity pressure. For this analysis, the first three items were fixed, and the cavity pressure was evaluated over the range from 10^{-4} to 10^{-1} torr (total pressure of constituents) to account for differing conditions appropriate for different driver methods.

The study showed the need for pumping capacities from 10^7 cfm (5×10^3 m^3/s) at 10^{-4} torr to 20,000 cfm (9.5 m^3/s) at 10^{-1} torr, and also provided a summary of vacuum system parameters for a 10^{-3} torr case. The high pumping capacity required in the high vacuum range indicates that the pumping systems would be too large to be practical, and that alternatives to direct pumping of the cavity only (e.g., zone pumping of the driver beam tube) should be assessed.

A cursory assessment of vacuum system major components indicated that the use of conventional vacuum pumps is applicable, albeit the required number may be high; but that other elements, such as a high-temperature lithium-compatible valve and a metal vapor condenser, will require development.

4.2 INTRODUCTION

Vacuum pumping is an integral part of all fusion devices and as such its design and that of the device should be carried out in parallel, so that the requirements unique to each particular fusion confinement concept are identified early. Each concept applies specific constraints on the vacuum system options. Conversely, vacuum system considerations, especially pumping capacity, can impact the selection of the fusion device operating point.

This preliminary evaluation of cavity pumping requirements for the HYLIFE fusion reactor concept serves to scope the vacuum pumping requirements for specific design point conditions, and shows the effect of the operating vacuum level on the required pumping capacity.

4.3 DESIGN CRITERIA

HYLIFE design criteria applicable to the vacuum pumping system were specified for this study and are shown in Fig. 4-1 and 4-2. Device operation is assumed to comprise a continuous series of 1-Hz shots, with the requirement to reestablish preshot conditions prior to each ignition. At pellet ignition (time, t = 0), the cavity equilibrium temperature is the temperature (500 °C) corresponding to the vapor pressure of the falling liquid lithium. A time span of 0.25 second was arbitrarily selected during which the lithium was heated, partly vaporized and recondensed, so that the lithium vapor temperature and that of the gases evolved as a result of the fusion shot was 1000 °C. This assumed temperature value was not expected to be exceeded at the start of pumping (t = 0.25 second). More likely, the temperature at this time will have recovered to

TIME HISTORY, SECOND	EVENT
0	CHAMBER EQUILIBRIUM TEMPERATURE = 500°C, PELLET IGNITION
0 TO 0.25	LITHIUM VAPORIZED & RECONDENSED. LITHIUM VAPOR CONTENT RETURNED TO PRESHOT LEVEL
0.25	TEMPERATURE = 1000°C
0.25 TO 1.0	CHAMBER PUMPED TO ESTABLISH PRESHOT CONDITION

R80-1210-021W

Fig. 4-1 Cavity Time History at 1-Hz Pulse Frequency

GAS	EVOLUTION, GRAMS/PULSE	PARTIAL PRESSURE INCREASE, TORR
DEUTERIUM	0.0074	2.09×10^{-4}
TRITIUM	0.0196	3.69×10^{-4}
HELIUM	0.0176	4.99×10^{-4}
HYDROGEN	0.0054 OR 0.152	3.05×10^{-4} OR 8.6×10^{-3}
TOTAL	0.05 0.195	–

INITIAL PRESSURE CONDITIONS

LITHIUM 3.6×10^{-3} TORR

OTHER GAS 10^{-4}, 10^{-3}, 10^{-2}, 10^{-1} TORR (FOUR CASES)

R80-1210-022W

Fig. 4-2 Design Criteria for Constituent Quantities & Pressures its initial value, and the assumption is conservative. The time period from t = 0.25 to 1.0 second was available for cavity pumping.

The gases evolved after each shot were hydrogen isotopes and helium in the proportions shown in Fig. 4-2. Two levels of hydrogen were evaluated to allow for uncertainty in the amount which might diffuse from the secondary intermediate loop. Preshot cavity pressures were chosen at values ranging from 10^{-4} to 10^{-1} torr (excluding lithium vapor pressure), so that pressure levels dictated by any particular beam injection method would be considered. Vacuum system data were elaborated at 10^{-3} torr to provide insight into possible system configurations. The cavity volume to be pumped, which is the difference between the cavity total volume and the volume occupied by the liquid lithium, was estimated at 700 m^3.

4.4 APPROACH

The total effective pumping speed requirement (i.e., at the vessel wall) was derived using the relationship for "pumpdown" of a cavity at a fixed pumping rate. The required partial pressure change from t equals 0.25 to 1.00 second was the summation of partial pressures calculated for the gas constituents (Fig. 4-2). The assumed vacuum system configuration (Fig. 4-3) consisted of numerous circular pumping ducts

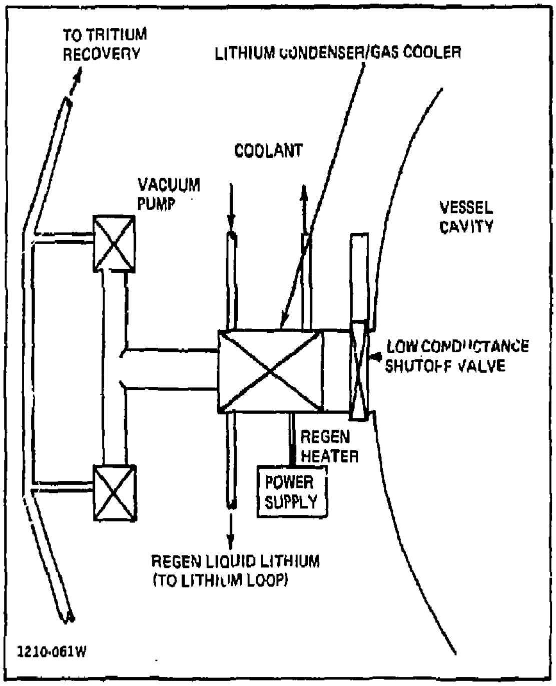

Fig. 4-3 HYLIFE Vacuum System Schematic Showing One Typical Location

extending radially outward from the vessel wall, with each duct having one or more pumps. The required pump speed at 25 °C was determined from the basic relationship for pumping at constant temperature, modified for the elevated cavity temperature in the cavity where the effective pumping speed is specified.

The basic relationship for a constant temperature system is:

$$\frac{1}{S_{eff_p}} = \frac{1}{C} + \frac{1}{S_p} \tag{4-1}$$

where

S_{eff_p} = effective pumping speed at the vessel wall for cavity temperature equal to gas temperature at the pump

C = pumping system conductance

S_p = pump speed

The cavity effective pumping speed (S_{eff}), for cavity temperature which is different from pump temperature, is derived from the root-temperature pumping relationship:

$$\frac{S_{eff}}{S_{eff_p}} = \left(\frac{T_c}{T_p}\right)^{1/2} \equiv TR \tag{4-2}$$

where T_c is the temperature in the cavity and T_p is the temperature of the constituents passing through the pump (25 °C). Combining the Eq 4-1 and 4-2 and defining K as the ratio of vacuum system conductance (C) to pump speed (S_p) gives:

$$S_p = \frac{K+1}{K} \cdot \frac{S_{eff}}{TR} \tag{4-3}$$

4.5 RESULTS

The results of the vacuum pumping systems analysis are shown in Fig. 4-4 for the selected design point (preshot partial pressure of the constituents = 10^{-3} torr) and in Fig. 4-5 for the parametric evaluation (preshot partial pressure range from 10^{-1} to 10^{-4} torr). The assumed configuration for the design point analysis consisted of 40 ducts of 3-ft (0.9-m) diameter, 10-ft (3-m) long. Duct conductances for this configuration were derived for the cases of high and low hydrogen content using average molecular weights. To satisfy the requirement to return to preshot pressure at t equals 1.0 second, the pumping requirement is one 25,000-cfm (12-m^3/s) pump per duct for the

PARAMETERS	LOW HYDROGEN	HIGH HYDROGEN
EVOLVED MASS PER PULSE, GM	0.05	0.195
AVERAGE MOLECULAR WT	4.09	2.28
PRESSURE RISE, TORR	1.4×10^{-3}	9.7×10^{-3}
INITIAL PRESSURE (EXCLUDING LITHIUM), TORR	10^{-3}	10^{-3}
EFFECTIVE PUMPING SPEED (1000°C), CFM (m^3/s)	1.6×10^6 (755)	4.4×10^6 (2000)
NO. OF PUMPING DUCTS (ASSUMED)	40	40
DUCT CONFIGURATION	3-FT DIA x 10 FT (0.9m DIA x 3m)	3-FT DIA x 10 FT (0.9m DIA x 3m)
REQUIRED PUMP SPEED/DUCT (25°C), CFM (m^3/s)	25,000 (12)	62,000 (28)
ASSUMED PUMPS/DUCT	1 x 25,000 CFM	2 x 30,000 CFM
TOTAL NO. OF PUMPS	40 @ 25,000 CFM	80 @ 30,000 CFM
DUCT CONDUCTANCE/PUMP SPEED	3.39	6.30

R80-1210-023W

Fig. 4-4 Vacuum Pumping System Definition for Selected Design Points

low hydrogen content case, and two 30,000-cfm (14-m^3/s) pumps (to use available sizes) per duct for the high hydrogen content case.

The parametric study results (Fig. 4-5) clearly show the effect on the pumping system of varying the required preshot pressure, and allude to the difficulty of restoring low operating pressures around the 10^{-4} torr range in the allotted 0.75-second because of the high pumping requirement. For this set of data, the value of the duct conductance to pump speed ratio (K) was chosen at 0.7, which implies small duct dimensions at the expense of larger pumps. The design point with 40 3-ft (0.9-m) diameter ducts points out the need for a reduced duct size; however, reducing the duct size below 2-ft (0.6-m) diameter would more than double the number of pumps.

It is intended that lithium vapor would not be passed through the vacuum system pumps. During the first 0.25 second after each shot, the vacuum system would be isolated from the cavity by a conductance limiter such as a valve qualified for high temperature service. During the pumping period after t equals 0.25 second, the bulk of the lithium vapor intersecting the first structural wall would condense on its relatively cool surfaces. Lithium entering the pumping ducts would be intercepted by condensers (baffle heat exchangers) in the ducts which would serve the dual purpose of dropping out the lithium and of precooling the other gas constituents before they enter the vacuum pumps.

The major vacuum system components consist of: a reasonably fast shutoff valve for high temperature service with lithium and tritium compatibility; a duct heat exchanger to condense lithium for separation and to cool gases from 1000 °C for pumping;

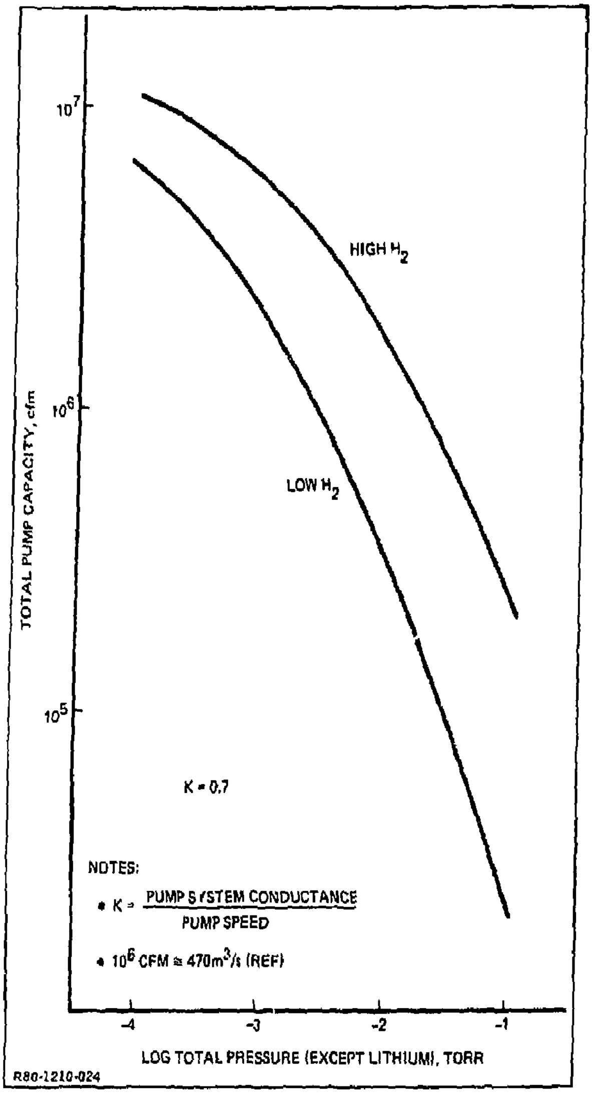

Fig. 4-5 Required Preshot Pressure Versus Pumping Capacity

a *medium range vacuum pump;* and hydrogen isotope/helium separation system for tritium recovery and accountability. The separation system is similar to the Tritium Systems Test Assembly (TSTA) currently being developed and assembled at the Los Alamos National Scientific Laboratory. All items except the vacuum pumps will require development; however, the TSTA program is applicable. Note that this system is not the primary tritium recovery system (neither for magnetic nor inertial confinement systems), and a system must be devised for tritium recovery from the lithium fall.

The design approach for this vacuum pumping system study was to apply pumping directly to the vessel cavity, and to maintain in the cavity the pressure required by the particular driver. The study has shown the problem of this approach, illustrated by the high pumping requirements and concomitant large system. It may be more appropriate to pump the driver tube directly and to satisfy an integral line density limit to be specified between the source and the pellet. This assessment is proposed for follow-on effort.

4.6 CONCLUSION

The vacuum pumping system configuration and its ability to satisfy the design criteria are clearly affected by the selected preshot cavity pressure, which is a function of the beam heating method. Lithium vapor incident on the vacuum pumping system is condensed by heat exchangers in the system; however, the system design is not strongly influenced by the selected liquid metal.

5 - SHOCK TUNNEL BLOWTHROUGH EXPERIMENT DESIGN

5.1 OVERVIEW

In an inertial confinement fusion reactor, a laser, electron or ion beam is focused onto a small pellet of deuterium-tritium (D-T) fuel. The extremely large beam energy flux on the surface of the pellet causes it to implode and release from 200 to 4000 MJ of thermonuclear energy. Pulses take place at a repetition rate of from 1 to 20 Hz. This energy, which is in the form of X-rays, neutrons, and particle debris, must be contained within the reactor cavity. The reactor structure must be protected from the blast and radiation. To implement this protection, a recent reactor structure design has a close-packed annular array of lithium liquid jets, which serve as a heat exchange medium for the energy of the D-T reaction, a tritium breeding mechanism, and protection for the structure. During a reactor pulse, X-rays and pellet debris generate, at the inner radius of the jets, a hot, high-pressure lithium plasma which implodes and subsequently flows radially outward in and around the jets towards the wall. In a practical reactor, the drag exerted on the jets must be small so as not to impart a large impulse to the jets and consequently a large impulse to the structure.

A quasi-one-dimensional analytical model and a computer code have been developed to describe plasma flow through a cylindrical array of jets and the subsequent impulse on the reactor wall (Subsection 5.10, Ref 5-1). Complete experimental verification of the code would be desirable, but the generation of the high temperatures and energies involved, plus the use of liquid lithium, would make such an experiment complex, time consuming, and expensive. However, a major portion of the code could be verified simply by means of experiments in the regime of low energy flow over simulated jets, where little disturbance would be imparted to the jets in the form of radiative transfer, erosion, or vaporization. This section describes the design of such an experiment which could be run in the Grumman Research Shock Tunnel. A major purpose of this experiment would be to measure the time-varying fluid pressure in the test section. Measurements would be made with and without the jet array present.

Subsection 5.2 outlines a number of potential test models for which the desired operating conditions are matched to shock tunnel operating conditions. In Subsection

5.3 the design of the preferred test section is discussed, and its jet array designs are presented in Subsection 5.4. Subsections 5.5, 5.6, and 5.7 discuss test section instrumentation, and Subsection 5.8 describes the test program and schedule.

5.2 SHOCK TUNNEL & TEST SECTION DESIGN CONDITIONS

The Grumman Research Department Shock Tunnel Facility is capable of operating over a wide range of stagnation (reservoir) temperatures and pressures using a wide variety of test gases. Figure 5-1 shows schematically the main features of the facility. Figures 5-2 and 5-3 show the shock tube portion of the facility, and some associated data recording and data reduction equipment.

For the HYLIFE blowthrough experiments being considered, argon is chosen as the test gas because its ratio of specific heats ($\gamma = 5/3$) is very close to that of the lithium vapor in the reactor, and it is ideally suited for use in shock-tube-type facilities (high molecular weight, inert, nontoxic, etc.). To avoid instrumentation problems with ionized flows, stagnation temperatures (T_5) are held below 8000 K. (Subscripts 2 through 5 refer to pressure regions in the tunnel.) Since the tunnel operates in the reflected shock mode, the incident shock Mach number (M_s) should not exceed approximately 6. Figure 5-4 shows the variation of T_5 as a function of M_s, and Fig. 5-5 shows the variation of stagnation pressure (P_5) as a function of M_s. Note that T_5 is independent of the pre-run pressure (P_1) in the tube because argon behaves as an ideal gas in the temperature range of interest, while P_5 is clearly a function of both P_1 and M_s. Figure 5-6 shows the diaphragm pressure ratio (P_4/P_1) necessary to achieve a given M_s assuming the driver gas is room temperature helium. Equations for the curves shown in Fig. 5-4, 5-5, and 5-6 can be found in standard texts on gas dynamics that describe shock tube flows. The present structural limitation on the driver tube and its gas supply system (plumbing, pumps, reservoirs, etc.) preclude operation at driver pressures over 30 MPa (300 atm) without some major facility modifications. This limit is plotted on Fig. 5-5. However, no basic fa-

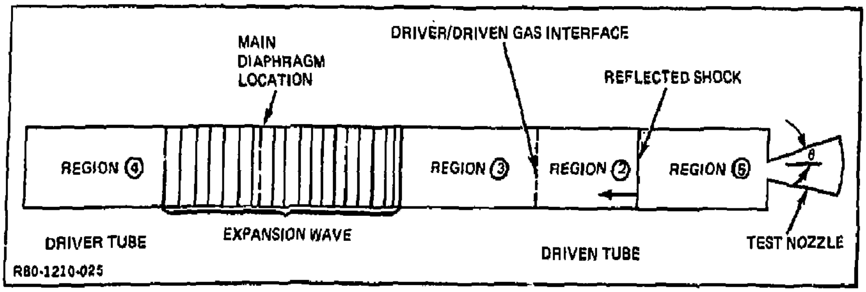

Fig. 5-1 Shock Tunnel/Test Nozzle Schematic

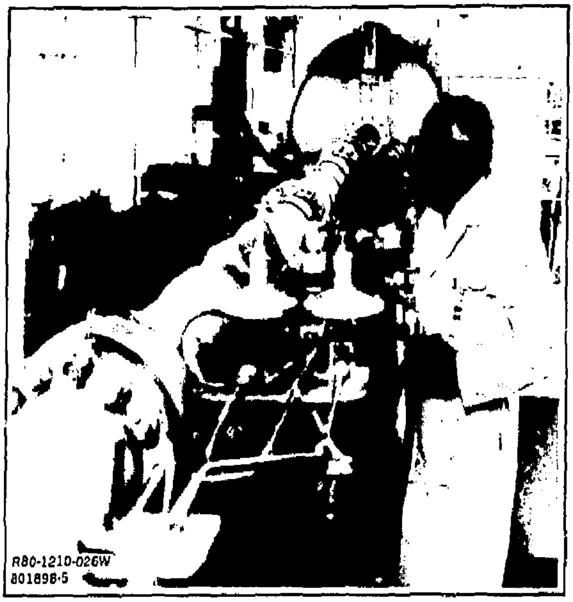

Fig. 5-2 Shock Tunnel Facility, Viewed from Driver Towards Vacuum Chamber

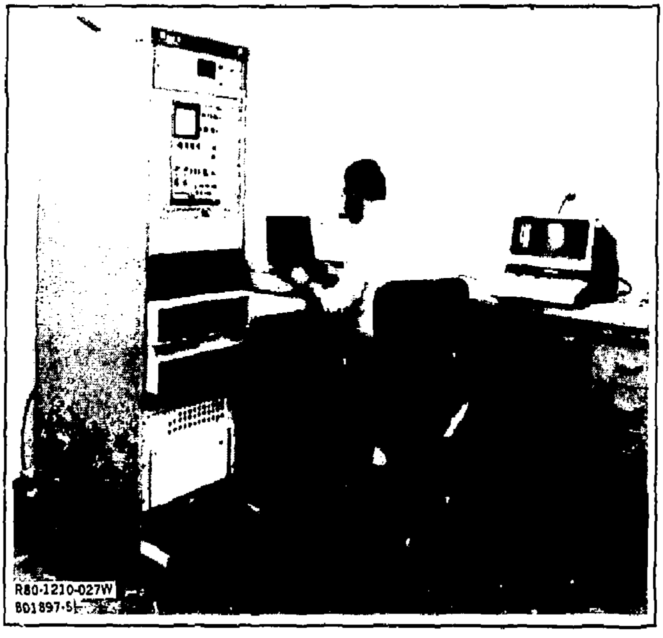

Fig. 5-3 Shock Tunnel Data Recording & Reduction Equipment, Including HP-1000 Computer, Multiplexer, Digital Oscilloscope, & Graphics Terminal

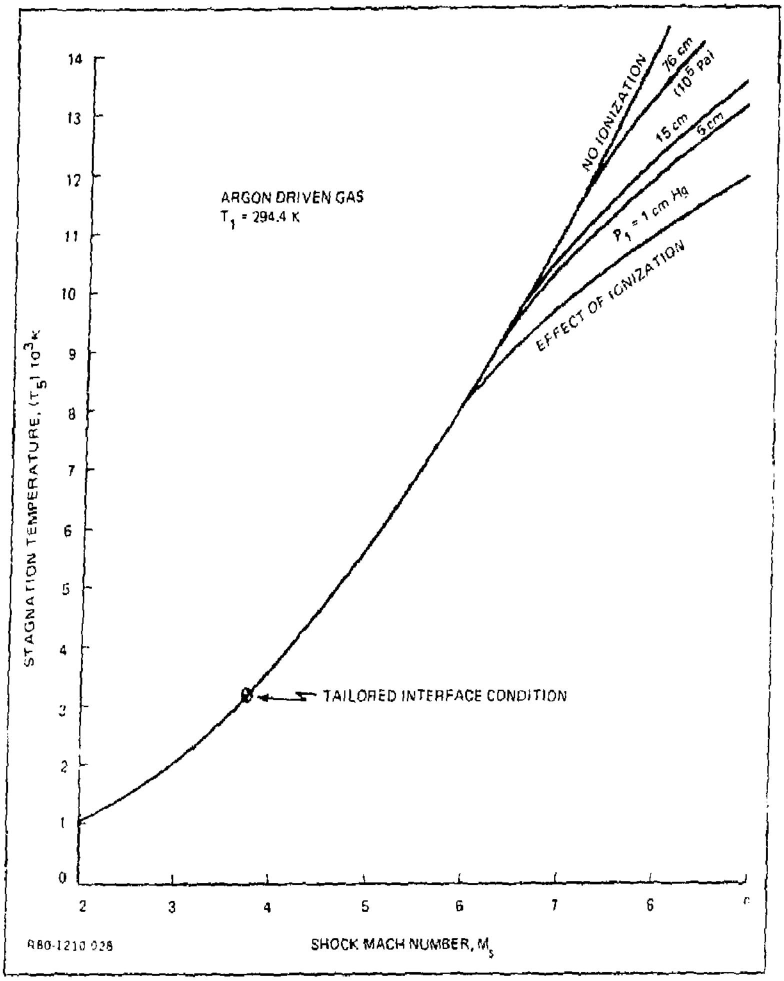

Fig. 5-4 Reflected Shock Tube Stagnation Temperature

cility modifications are needed for proposed tests, because the present range of performance will satisfy the test objectives.

Figures 5-4, 5-5, and 5-6 also show an operating point called the "tailored interface condition". This term refers to the interaction of the reflected shock wave with the driver gas/driven gas interface. Generally, when a shock wave interacts with a gaseous interface, a wave is transmitted across the interface and another wave is reflected. If the acoustic impedance mismatch at the interface is zero, the transmitted wave continues with no change in strength from the impinging wave, and the reflected wave is infinitesimally weak, i.e. a Mach wave. In a shock tube, for any given driver

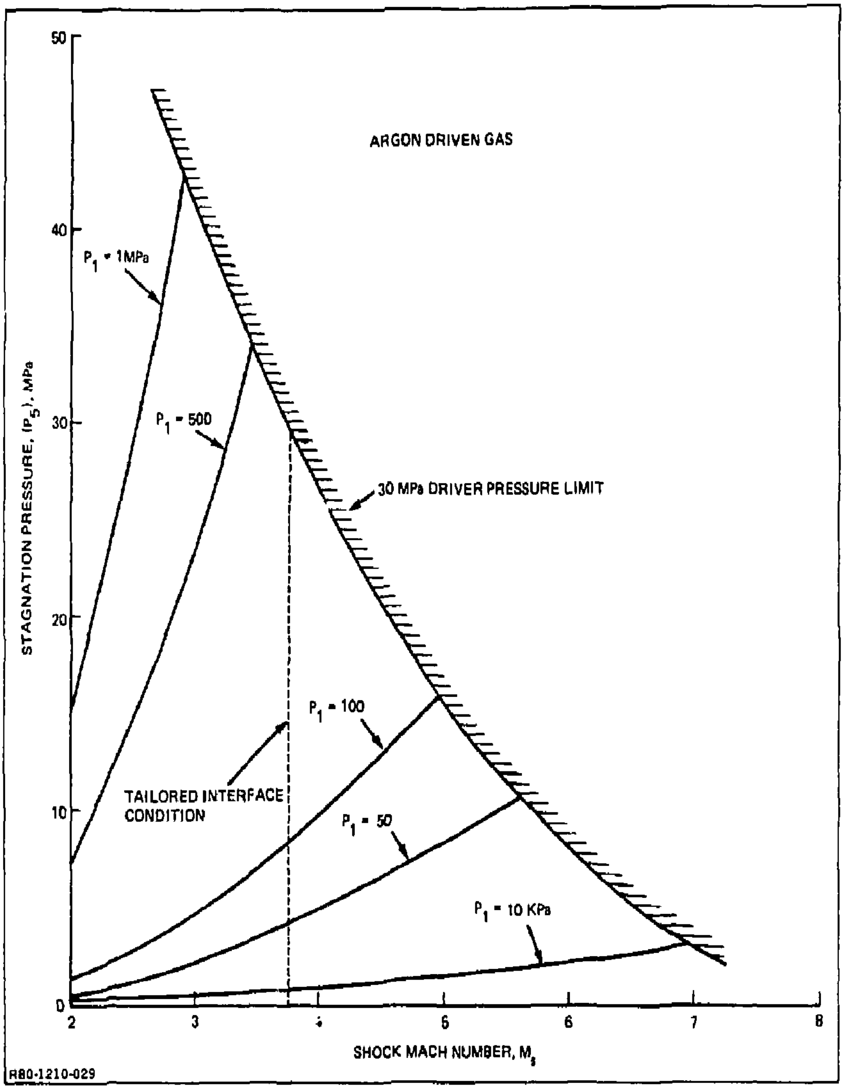

Fig. 5-5 Reflected Shock Tube Stagnation Pressure

gas/driven gas initial conditions, there is only one incident M_s for which the impedance jump across the interface is zero. This condition is called the tailored interface condition. It has a significant effect on the available testing time in a reflected shock tube, which is illustrated in Fig. 5-7 and 5-8.

Figure 5-7 is a standard shock tube distance-time diagram, drawn for the Grumman shock tube (6-m (20-ft) driver tube length and 10-m (33-ft) driven tube length), but at the tailored interface running condition. Note that the reflected shock wave

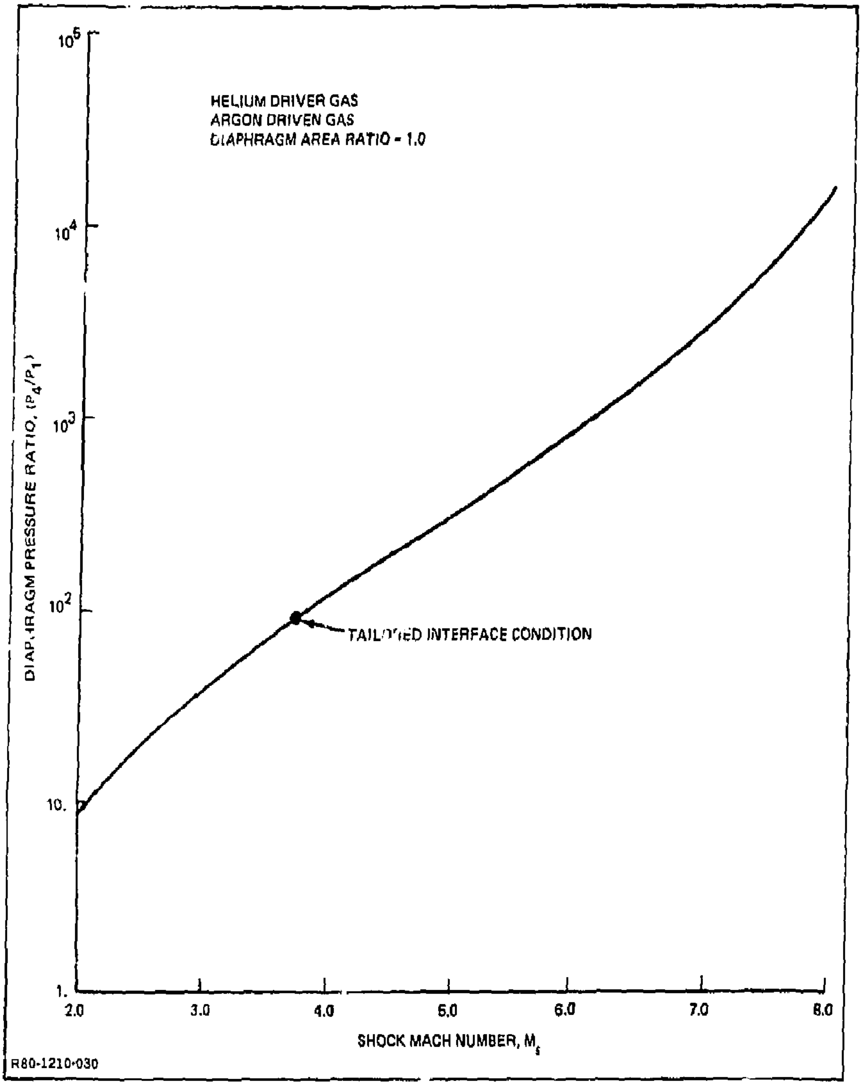

Fig. 5-6 Diaphragm Pressure Ratio

passes through the interface with no change in speed and with no reflected disturbance propagating back into Region 5. The testing time (about 10 ms in this case) is terminated by the arrival at the end wall of the reflected expansion wave from the driver. At any other incident shock wave speed, a new wave, propagating back into Region 5, would be generated at the point where the reflected shock wave intersects the interface, which would considerably shorten the available testing time. Figure 5-8 illustrates this point quantitatively. The curve gives the testing time available

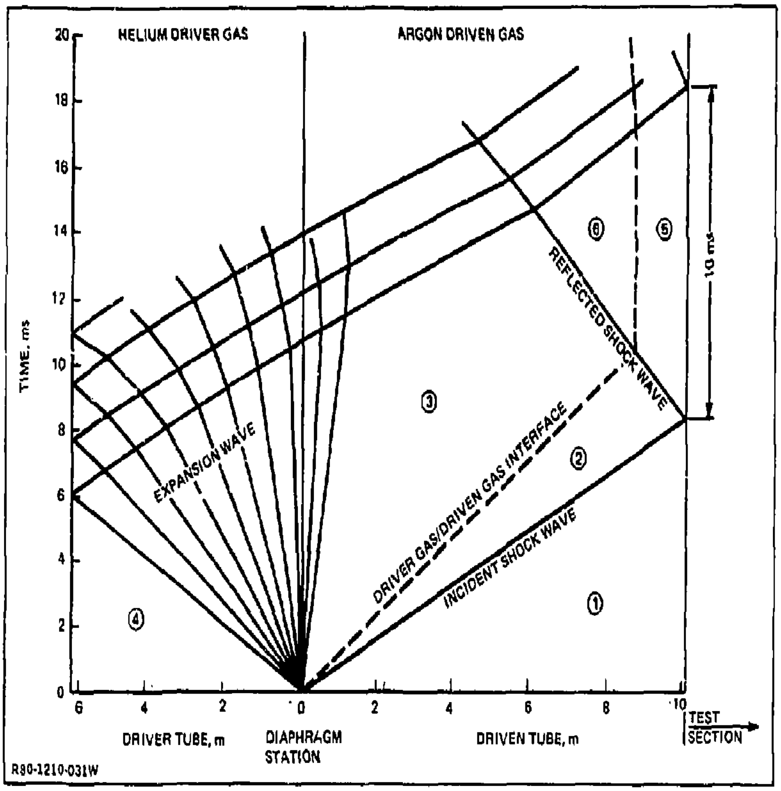

Fig. 5-7 Distance-Time Diagram for Tailored Interface Condition

in a helium/argon reflected shock tube with a 10-m (33-ft) long driven tube. At one particular shock Mach number ($M_s = 3.75$ in this case), the interface is tailored and there is a significant jump in the available testing time. The equation for the curve shown in Fig. 5-8 is given by:

$$\Delta t = \frac{X_1}{U_s}\left[\left(\frac{\rho_{51}-1}{\rho_{51}}\right)\left(\frac{\rho_{21}}{\rho_{21}-1}\right)-1\right]+\frac{X_1}{U_{RR}\rho_{51}} \qquad (5\text{-}1)$$

where

$$\rho_{51}=\frac{\rho_5}{\rho_1}\,;\ \rho_{21}=\frac{\rho_2}{\rho_1}$$

and X_1 = length of driven tube

U_s = velocity of incident shock wave

ρ_i = density in Region i

U_{RR} = velocity of reflected disturbance from interface propagating back into Region 5

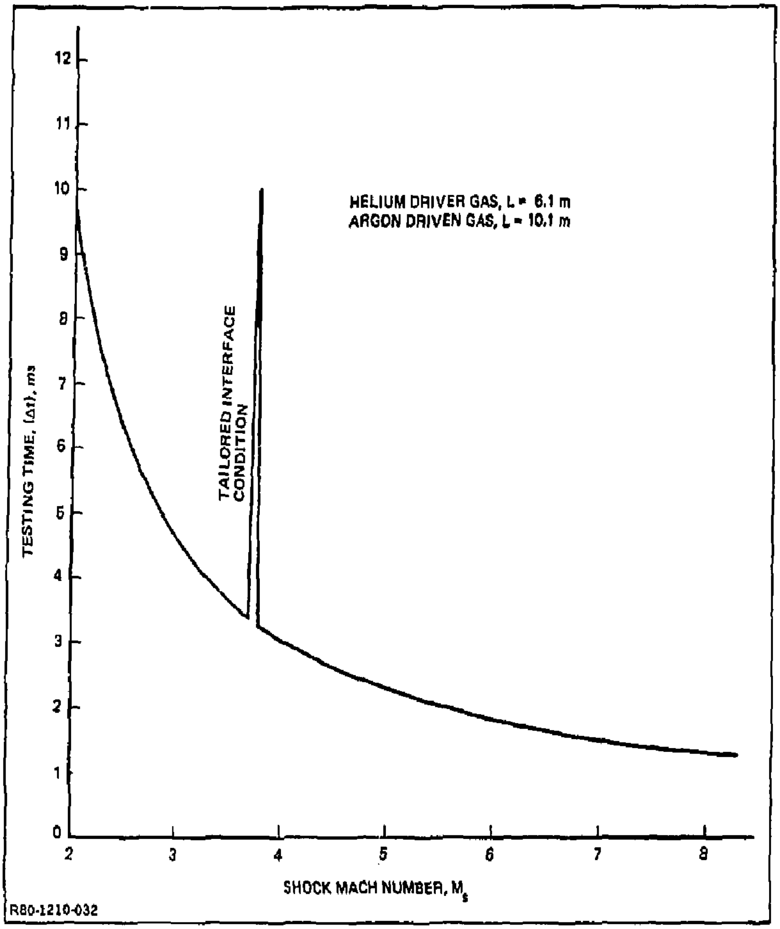

Fig. 5-8 Reflected Shock Tube Testing Time

For incident M_s less than the tailored condition, the reflected disturbance propagating back into Region 5 is an expansion wave, and U_{RR} equals the speed of sound (a_5) in Region 5. For higher M_s the reflected disturbance is a shock wave and U_{RR} equals $M_5 a_5$, where M_5 is the Mach number of the shock wave.

The condition for tailoring is given by the parameter:

$$E_{32} - \frac{\alpha_3 + P_{25}}{\alpha_2 + P_{25}}$$

where

$$E_{32} = \frac{E_3}{E_2} = \frac{C_{v3} T_3}{C_{v2} T_2} \ ; \quad P_{25} = \frac{P_2}{P_5} \ ; \quad \alpha_i = \frac{\gamma_i + 1}{\gamma_i - 1}$$

and C_{v_i} = specific heat at constant volume in Region i

T_i = temperature in Region i

P_i = pressure in Region i

γ_i = ratio of specific heats in Region i

When this parameter is less than zero, the reflected disturbance at the interface is an expansion wave. When the parameter equals zero, the disturbance is a Mach wave (zero strength wave), and when the parameter is greater than zero, the disturbance is a shock wave.

The stagnant shock heated and pressurized gas in Region 5 bursts a thin diaphragm at the end of the shock tube, and then expands through a two-dimensional convergent/divergent nozzle to a supersonic Mach number. The array of jets (steel rods for simulation) is located downstream in the nozzle, which is terminated by an end-wall from which the flow (shock waves) reflects and propagates back upstream over the jets. It is the passage of the flow through the array of jets and the following reflected flow phenomena that is intended to be studied experimentally. Figure 5-9 illustrates the proposed physical flow test model.

To rationally design the jet array model, the basic flow phenomena that occurs in a two-dimensional conical nozzle was analyzed. Arbitrarily, two different expansion angles were chosen, where the nozzle half angles (θ) equal 5 and 15 deg. Figure 5-10 is a distance-time diagram illustrating the main features of the flow. If a nozzle is initially highly evacuated, the first pulse of gas will move through the nozzle at the limiting unsteady thermodynamic velocity (U_{LIM}) given by:

$$U_{LIM} = \frac{2}{\gamma - 1} a_5 \tag{5-2}$$

This velocity is essentially independent of the nozzle expansion angle. Following this initial pulse is an unsteady flow of gas in which the pressure builds up and the velocity slows down to the values given by the steady flow conservation equations. In wind tunnel testing, this unsteady flow region is referred to as the "starting" phenomenon, and it must be swept through the test section before steady flow testing can take place. The trailing edge of this unsteady portion of the flow has the velocity ($U_\infty - a_\infty$) where the ∞ subscript refers to the local free stream conditions. Steady

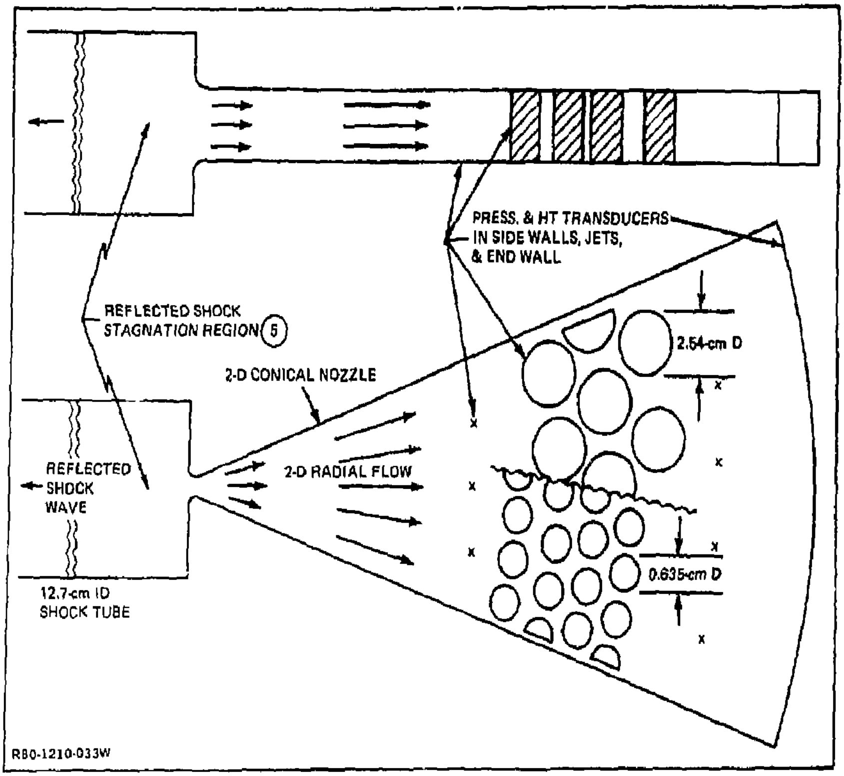

Fig. 5-9 Steady Supersonic Flow Model

flow begins after the passage of this wave. The steady flow Mach number (M_∞) is directly related to the area ratio of the expansion by the equation:

$$\left(\frac{A_\infty}{A_*}\right)^2 = \frac{1}{M_\infty^2}\left[\frac{2}{\gamma-1}\left(1+\frac{\gamma-1}{2}M_\infty^2\right)\right]^{\frac{\gamma+1}{\gamma-1}} \tag{5-3}$$

Where the * subscript refers to the throat (sonic) condition. In a two-dimensional conical nozzle, the area ratio is a function of the expansion angle and the nozzle length, given by:

$$\frac{A_\infty}{A_*} = \frac{X_\infty \tan\theta}{h_*} + 1 \tag{5-4}$$

where

X_∞ = nozzle length measured from throat

θ = nozzle half angle

h_* = nozzle throat half height

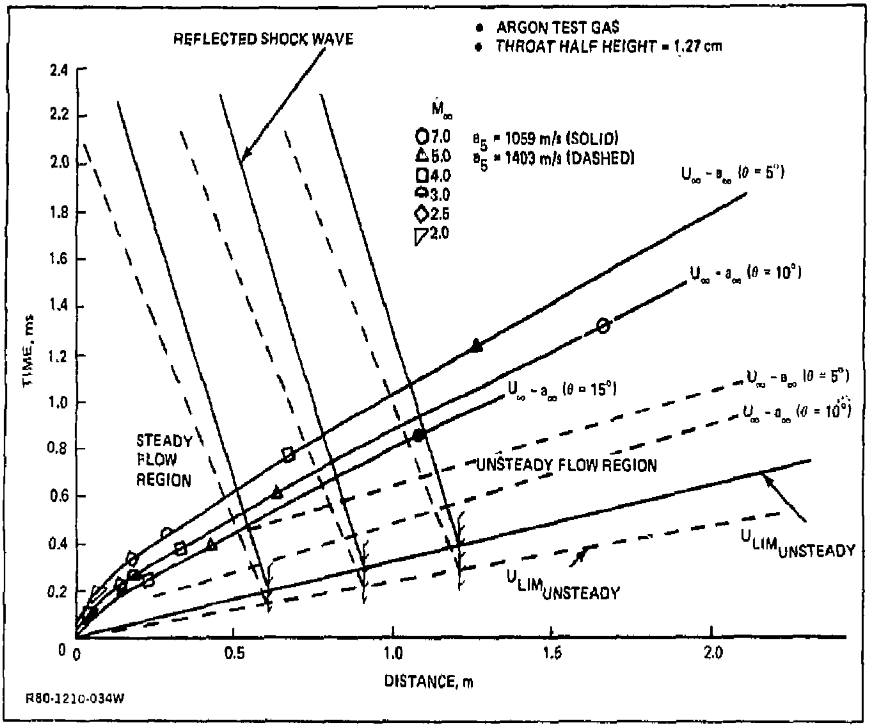

Fig. 5-10 Test Section Distance-Time Diagram for Tailored Interface Condition with *Various Nozzle Expansion Angles*

Consequently, the "starting" wave ($U_\infty - a_\infty$) is a function of the nozzle expansion angle, and the steady free stream Mach number (M_∞) is a function of both the expansion angle and the distance from the throat. These points are illustrated in Fig. 5-10. Since wave speeds and velocities also are proportional (to some power) to the stagnation temperature of the flow, U_{LIM} and ($U_\infty - a_\infty$) are plotted for two different stagnation conditions; namely, the tailored condition where a_5 equals 1059 m/s (3475 ft/s), and for an M_S of 5, where a_5 equals 1402 m/s (4601 ft/s). The former is shown as solid lines and the latter as dashed lines.

The calculation of the wave that reflects from the nozzle end wall and the flow field behind it is, at best, highly speculative. The wave is advancing into a converging channel through an unsteady flow medium. A simplified analysis was made assuming the wave speed was that obtained for a wave advancing into a uniform region where mass flow equals throat mass flow with steady flow properties behind the wave, i.e. no axial gradients between the wave and the end wall. The flow in the test nozzle was modeled as a cylindrical supersonic source flow. An expression for the velocity as a function of distance (from Ref 5-2) is:

$$U^2\left[\frac{4-U^2}{3}\right]^3=r^{-2} \tag{5-5}$$

where

$$U=\frac{U_1}{U_*}\ ;\ r=\frac{r_1}{r_*}$$

The quantities U_1 and r_1 are the local velocity and radial distance, and U_* and r_* are the sonic velocity and position within the test nozzle.

An approximate calculation of the return shock speed is made in a cylindrical supersonic source flow. The assumption is made that the fluid reaches the limiting velocity ($M = \infty$) throughout the flow field. For this case, the ratio of the density upstream of the shock to the density in the stagnation Region 5 is (see Fig. 5-11):

$$\frac{\rho_1}{\rho_5}=\frac{\left(\frac{2}{\gamma+1}\right)^{\frac{\gamma+1}{2(\gamma-1)}}}{\left(\frac{2}{\gamma-1}\right)^{1/2}}\quad\frac{r_*}{r_1} \tag{5-6}$$

For the case where the fluid has reached the limiting velocity, the density behind the shock at Region 1 is:

$$\rho_s\approx\frac{\gamma+1}{\gamma-1}\rho_5\left(\frac{\rho_1}{\rho_5}\right) \tag{5-7}$$

Equating the throat fluid throughput in a time (t) to the accumulated fluid mass behind the upstream propagating shock yields:

$$\int\rho_s dV=\dot{m}t=\rho_* U_* A_* t \tag{5-8}$$

Expressing the throat conditions on the right-hand side of Eq 5-8 in terms of Region 5 stagnation conditions, and integrating the left-hand side of Eq 5-8 with Eq 5-6 and 5-7

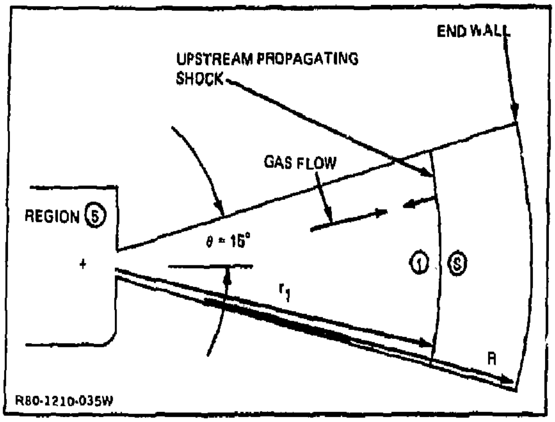

Fig. 5-11 Cylindrical Source Flow Model

between the shock position (r_1) and the end wall (R); an expression for the upstream propagating shock position as a function of time is obtained:

$$r_1 = \left[\frac{\left(\frac{\gamma - 1}{2}\right)^{1/2}}{(\gamma + 1)} a_5 \right] t + R \tag{5-9}$$

where the bracketed term in Eq 5-9 is the upstream propagating shock speed. This wave is shown plotted in Fig. 5-10 for three different end wall locations and for the two values of a_5. From Fig. 5-10 it can be seen how much steady (and unsteady) flow would be expected for various nozzle angles, nozzle lengths, and jet array locations, as well as for two different shock tube operating conditions. The available steady flow times will be in the order of 1 or 2 ms which means that testing times will be limited by wave reflections in the nozzle rather than in the shock tube. More importantly, even for a nozzle as short as 60 cm (2 ft), there should be sufficient time for the flow to establish over the arrays and for measurements to be made.

Point designs taken from the parametric design curves are shown in Fig. 5-12. Two test nozzles were considered with nozzle expansions angles of 5 and 15 deg. The test nozzle length was 60 cm (2 ft). Shock Mach numbers of 3.75 and 5.0 were considered. The test nozzle test times vary between 0.8 and 1.2 ms. The available test time was 2.0 ms or greater. The Region 5 stagnation pressures and temperature remained constant over the available test time. There are three Region 5 stagnation pressures for each stagnation temperature which corresponds to three different driven

PARAMETER	VALUES				
SHOCK MACH NUMBER	3.75	3.75	5.0	5.0	3.6
TEST NOZZLE EXPANSION HALF ANGLE (θ), DEG	5	15	5	15	15
MACH NUMBER AT JETS	3.0	4.5	3.0	4.5	3.0**
SHOCK TUNNEL AVAILABLE TEST TIME*, ms	10.0	10.0	2.3	2.3	3.4
TEST NOZZLE TEST TIME, ms	1.0	1.2	0.8	0.95	–
TIME OF INITIAL PULSE AT NOZZLE END WALL, ms	0.2	0.2	0.15	0.15	–
TIME OF REFLECTED SHOCK OVER JETS, ms	1.2	1.4	0.95	1.1	–
SHOCK TUNNEL STAGNATION TEMP (T_5), K	3230	3230	5665	5665	2800
SHOCK TUNNEL STAGNATION PRESS. (P_5), 10^5 Pa					
$P_1 = 0.1 \times 10^5$ Pa	8.5	8.5	16	16	–
$P_1 = 1.0 \times 10^5$ Pa	85	85	160	160	–
$P_1 = 2.0 \times 10^5$ Pa	170	170	–	–	280 ‡

* AT REGION 5

** LDV, IR TEMP LOCATION 13 cm FROM TEST SECTION THROAT

‡ $P_1 = 4 \times 10^5$ Pa

TEST NOZZLE LENGTH	– 0.61m	INITIAL DRIVER GAS TEMP	– 294.4K
TEST JET LOCATION (CENTER OF ARRAY)	– 0.305m	INITIAL DRIVEN GAS TEMP	– 294.4K
DRIVER GAS	– HELIUM	DRIVER TUBE LENGTH	– 6.1m
DRIVEN GAS	– ARGON	DRIVEN TUBE LENGTH	– 10.1m

1210-053W

Fig. 5-12 Shock Tunnel Parameters for Low Energy HYLIFE Reactor Verification Experiment

tube initial pressures (P_1). The 5-deg expansion nozzle will be a little easier to handle during a test because it can be slid free of the dump tank without dismantling from the driven tube.

To accommodate a Laser Doppler Velocimeter (LDV) and infrared (IR) measurements of velocity and temperature downstream of the throat, a fifth shock tube running condition was considered. For this condition (Fig. 5-12), the incident M_s was 3.6, the driven tube pressure was 400 kPa (4 atm), and the resulting Region 5 pressure was 28 MPa (280 atm).

5.3 SHOCK TUNNEL MODEL DESIGN

Figure 5-13 is a preliminary drawing (used for cost estimating purposes) showing the proposed blowthrough model design. The internal flow channel is basically a 30-deg sector of a right-circular cylinder, 25-mm (1-in.) thick. It attaches to the end of the existing 125-mm (5-in.) id shock tunnel driven tube by means of a 27-cm (10-1/2-in.) diameter bolted flange. Internally, this flange contains the thin diaphragm which separates the initial driven tube gas from the initial vacuum in the model, as well as

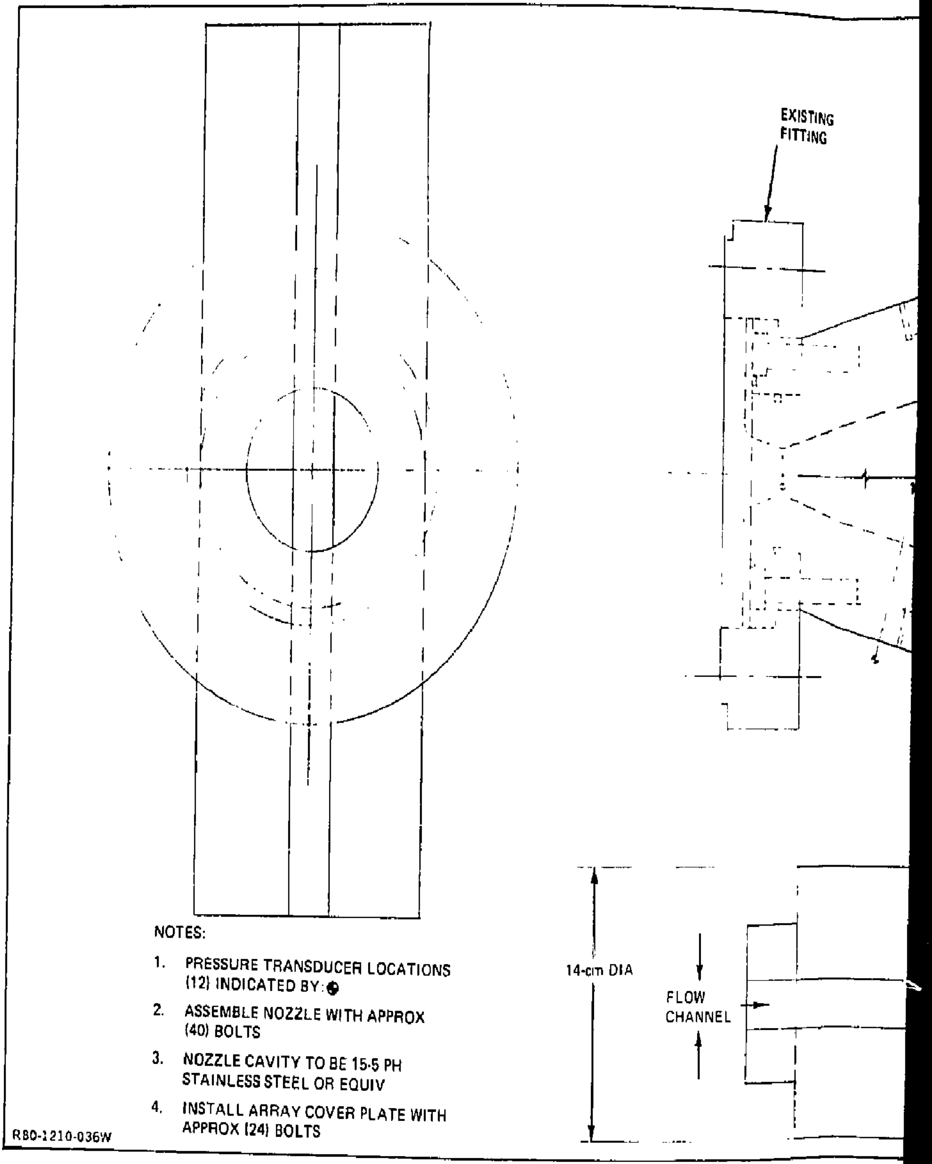

NOTES:

1. PRESSURE TRANSDUCER LOCATIONS (12) INDICATED BY: ⊕
2. ASSEMBLE NOZZLE WITH APPROX (40) BOLTS
3. NOZZLE CAVITY TO BE 15-5 PH STAINLESS STEEL OR EQUIV
4. INSTALL ARRAY COVER PLATE WITH APPROX (24) BOLTS

R80-1210-036W

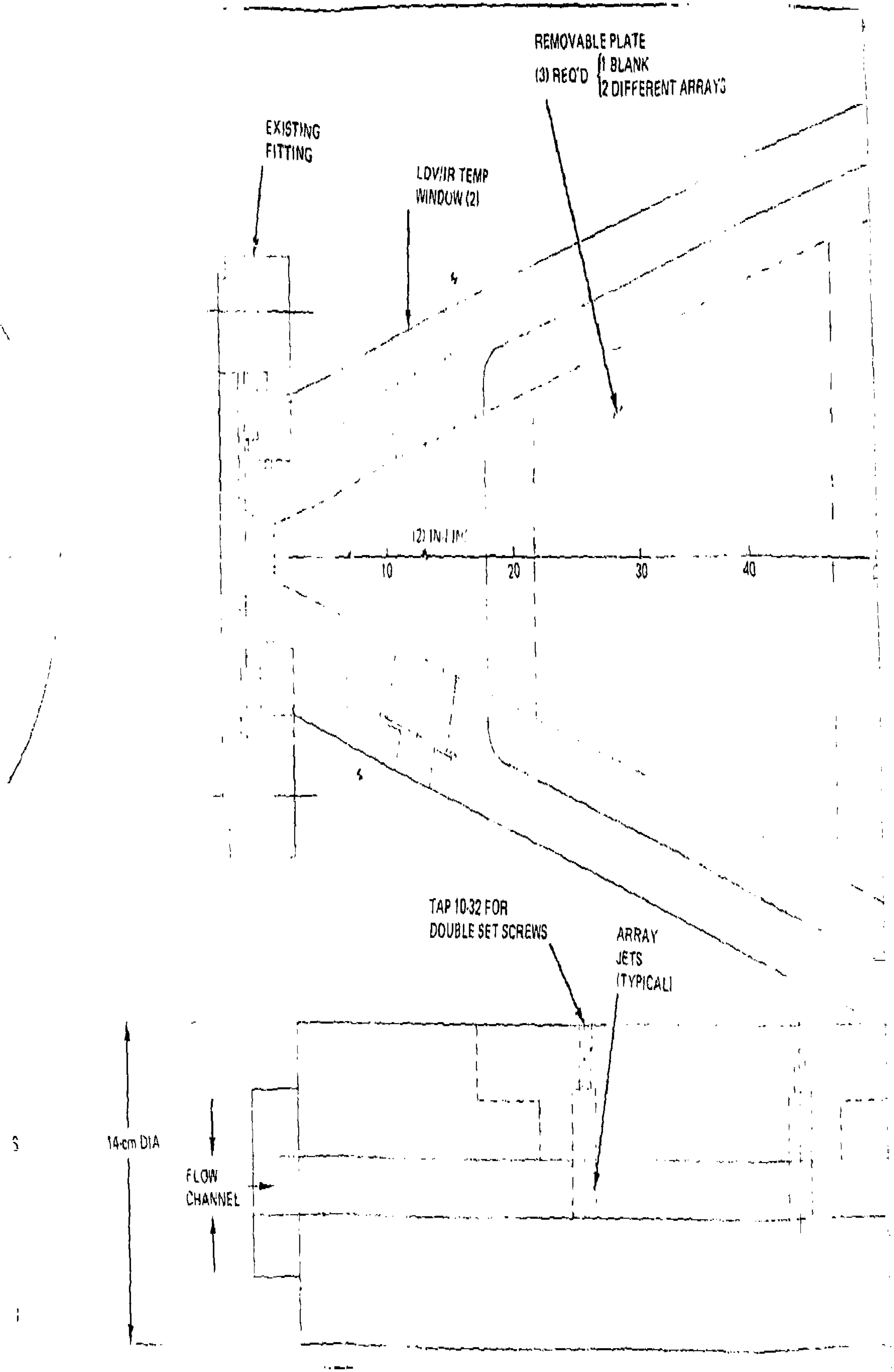
REMOVABLE PLATE
(3) REQ'D
1 BLANK
2 DIFFERENT ARRAYS
EXISTING FITTING
LDV/IR TEMP WINDOW (2)
(2) IN-LIN
10
20
30
40
TAP 10-32 FOR DOUBLE SET SCREWS
ARRAY JETS (TYPICAL)
14-cm DIA
FLOW CHANNEL

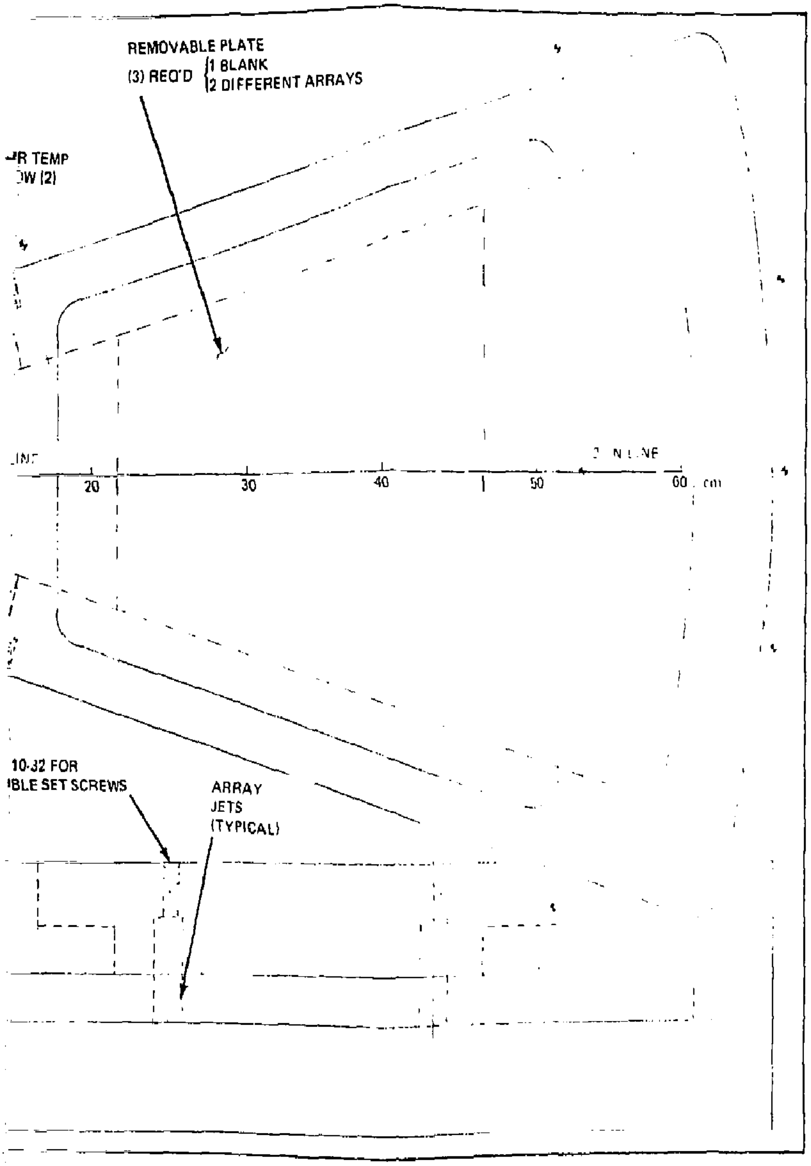

Fig. 5-13 Blowthrough Experiment Shock Tunnel Model

the converging channel which accelerates the shock processed driven tube gas to sonic conditions at the model throat (minimum cross-section area). The jet array is located about midway down the 60-cm (2-ft) length of the 30-deg diverging sector of the model. The simulated jets (steel rods) are mounted in a removable access plate. The intent is to make three different access plates: one with no jets, and two with different jet diameters and array sizes (refer to Subsection 5.4). The circular arc end wall of the model is designed so it can be moved closer to the last row of jets, thus shortening the internal-flow portion of the model and allowing the distance from the last row of jets to the end wall to be an experimental variable. All internal-flow surfaces are ground and polished to at least a 810-nm (32-μin.) finish.

Pressure will be measured at 12 different locations on the model; five ahead of the jet array and seven aft of the array and on the end wall. Transducer port placement will enable tracking the passage of the various shock waves within the model, and resulting wave speed data will be used in diagnosing the flow properties as a function of time.

There will be two windows for optical diagnostic measurements upstream of the jet array, flush mounted with the model internal surface to minimize flow disturbances.

Subsections 5.5 to 5.7 on instrumentation (Pressure Transducers, LDV, and IR Temperature Measurement) give details of all the proposed measurements and the required instrumentation.

The model will be mounted horizontally (i.e. the 30-deg expansion will be in the horizontal plane) within the shock tunnel vacuum chamber. This chamber has a sliding vacuum seal at one end that accepts the end of the driven tube and two 45-cm (18-in.) diameter windows for optical diagnostics and for viewing the model. The circular arc end wall of the model will have a solenoid-operated dump valve attached and safety blowout burst discs. The solenoid valve will be open initially, allowing the model to be evacuated by pumping out the tunnel vacuum chamber. (Pressures in the mPa (10^{-5} torr) range are easily attainable in this chamber.) The solenoid valve will be closed before the run to eliminate any flow disturbance that might be caused by an opening in the end wall of the model. The burst discs will be set to blow open at a pressure level achieved after the "data-taking" time period of the run. They will protect the sensitive pressure transducers and window seals from the high overpressures in the shock tunnel at the end of a run.

5.4 JET ARRAY DESIGN

The simulated array of jets for the proposed tests was designed to match as closely as possible the cross-section area distribution shown in Figure 3 of Ref 5-1. The gross features of that figure were replotted as the percent (or fraction) of open area versus radial distance, and the results are shown in Fig. 5-14. This figure shows two significant features; namely, that the minimum open area (maximum blockage) is essentially independent of radial position (≈ 40%), and that the maximum open area (minimum blockage) also is independent of radial position (≈ 65%). This enabled computing the location of a series of overlapping rows of circular jets. The maximum opening between any two jets in any one row was 65% of the distance between their centers, and the minimum open area between two overlapping rows of jets was 40% of the projected distance between their centers. The geometry of this arrangement is shown in Fig. 5-15. Admittedly, this does not match precisely the geometry presented in Ref 5-1, but it does give a rational scheme to closely approximate the blockage distribution of Ref 5-1 with different jet diameters and jet array sizes that are mathematically scaled. The assumptions implicit in this analysis are:

- All jets are circular in cross-section, equal in diameter, and uniformly spaced in each row
- The simulated array can be started and terminated at any arbitrary radial location, because the maximum and minimum open area fractions are independent of radial position.

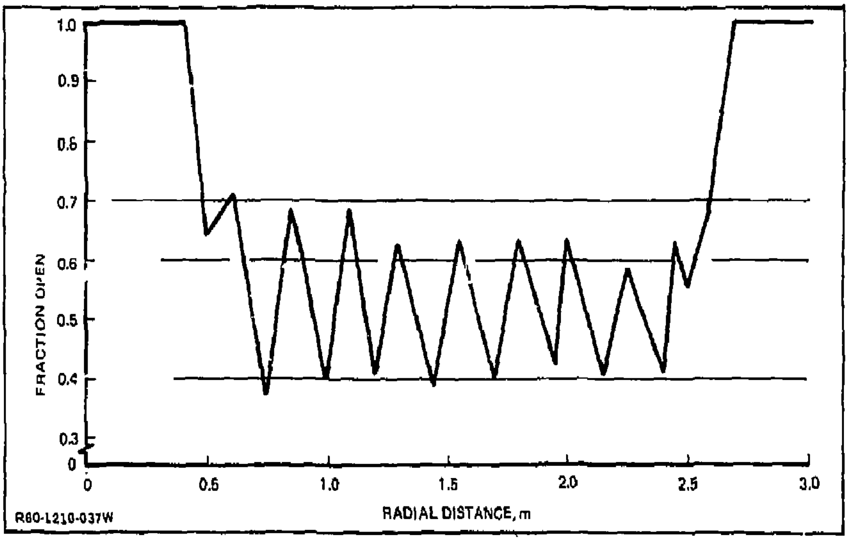

Fig. 5-14 Jet Array Area Distribution

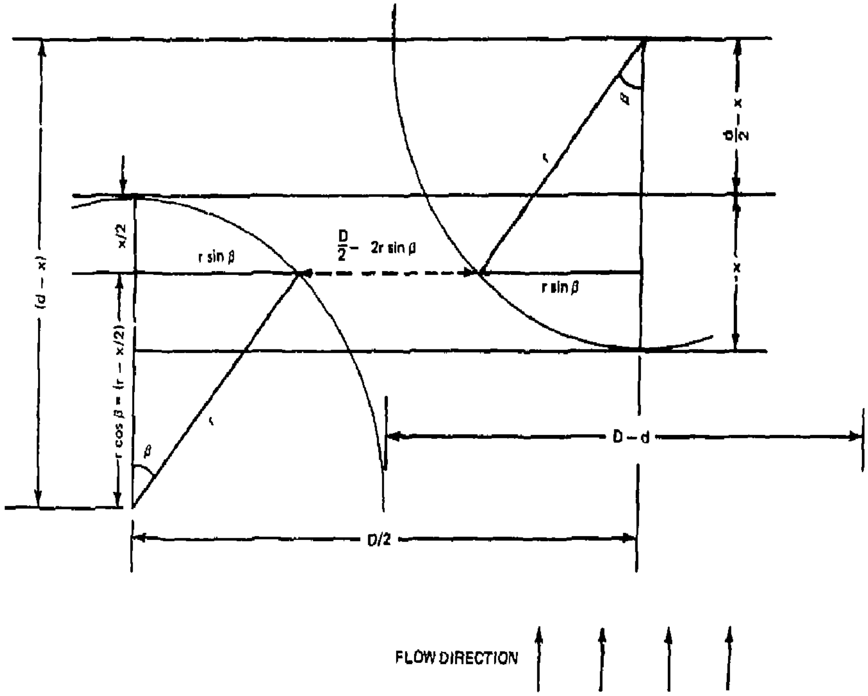

$$d = 2r$$

$$\frac{D-d}{D} = \text{MAXIMUM FRACTION OPEN BETWEEN JETS IN ANY ONE ROW}$$

$$D = \frac{d}{(1 - \text{FRACTION OPEN}_{\text{MAX}})}$$

$$\frac{\frac{D}{2} - 2r\sin\beta}{D/2} = 1 - \frac{2d\sin\beta}{D} = \text{MINIMUM FRACTION OPEN BETWEEN SUCCESSIVE ROWS}$$

$$\sin\beta = \frac{D}{2d}(1 - \text{FRACTION OPEN}_{\text{MIN}})$$

$$r\cos\beta = r - \frac{x}{2}$$

$$\cos\beta = \frac{d-x}{d}$$

$$x = d\,(1 - \cos\beta)$$

R80-1210-038W

Fig. 5-15 Model Jet Array Geometry

Figure 5-16 gives the results of calculations made for several jet diameters, assuming a maximum open fraction between jets of 0.65 and a minimum open fraction of 0.4. The proposed plan is to test only the two larger diameter jet arrays.

In the geometry shown in Fig. 5-15, the jets in the second row are shown located halfway between the two jets of the preceding row. This produces a poor arrangement, because in this case (65% minimum blockage and 40% maximum blockage), D is greater than 2d, where D is the distance between jet centers in any one row and d is the jet diameter. This leads to unimpeded, open channels (lines of sight) between the jets in the flow direction. The analysis is still valid if the jets in successive rows are not centered between the jets of the preceding row, but are staggered. This alleviates the direct line-of-sight problem, but can still lead to preferred channels of flow if the staggering is done improperly. Figure 5-17 shows a proposed layout of 13-mm (1/2-in.) diameter jets where the staggering is arranged to eliminate any obvious preferred channels of flow.

5.5 PRESSURE TRANSDUCERS

To specify the pressure transducer used to measure the transient pressure in the test nozzle during a run, it is necessary to calculate the approximate test nozzle pressure distribution as a function of time.

Qualitatively, the flow in the test nozzle develops in the following manner: when the mylar diaphragm at the test section entrance ruptures, the gas expands down the test section at the limiting thermodynamic velocity to the end wall; this initial gas

	JET DIAMETER			
PARAMETER	1.905	1.270	0.953	0.635
DISTANCE BETWEEN CENTERS IN EACH ROW (D)	5.443	3.630	2.720	1.814
OPEN DISTANCE BETWEEN CENTERS IN EACH ROW (D – d)	3.538	2.360	1.768	1.179
OVERLAP BETWEEN SUCCESSIVE ROWS (x)	0.925	0.615	0.462	0.307
DISTANCE BETWEEN CENTERS IN SUCCESSIVE ROWS (d – x)	0.980	0.655	0.490	0.328

NOTE: ALL DIMENSIONS IN CENTIMETERS
MAX FRACTION OPEN = 0.65
MIN FRACTION OPEN = 0.40

1210-054W

Fig. 5-16 Jet Array Parameters

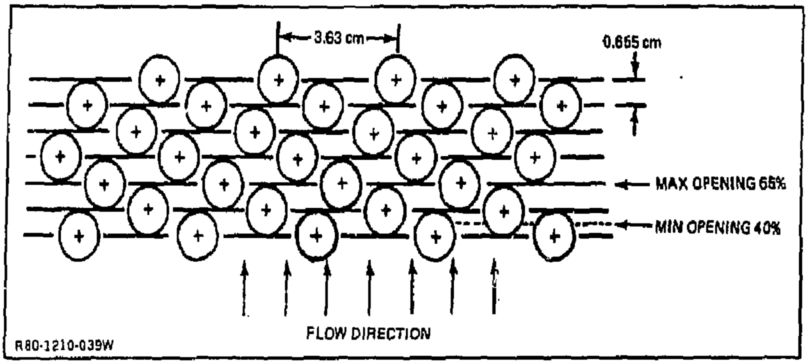

Fig. 5-17 Proposed Jet Array for ½-Inch (1.27-cm) Diameter Jets

front stagnates on the end wall and a shock wave forms, which reflects upstream to the nozzle throat.

A characteristic time for the test is from the initiation of the test nozzle flow until the upstream propagating shock passes the jet array midpoint which is midway between the test nozzle throat and the end wall.

Calculations of the pressure on the end wall will be made twice; initially when the upstream propagating shock wave is at the end wall, and again at the midpoint location of the jet array.

The end wall pressures for those cases when the upstream propagating shock is at the two locations stated above is given in Fig. 5-18. The time at which the pressure occurs is determined from Fig. 5-10. The calculations were made for a divergence half angle θ of 15 deg, and for two driven tube initial pressures (P_1) of 100 and 10 kPa (1.0 and 0.1 atm). The corresponding values of the Region 5 stagnation pressure are 16 and 1.6 MPa (160 and 16 atm). Also, pressures were calculated at two locations between the throat and the jet array for those conditions when the nozzle flow reaches steady state. The calculations were made for locations corresponding to free stream Mach numbers of 2.0 and 3.0, and for a Region 5 stagnation pressure of 16 MPa (160 atm). The time for the flow to reach steady state at these locations is of the order of

END WALL			UPSTREAM OF JET ARRAY	
	PRESSURE		PRESSURE	
TIME, ms	$P_1 = 1.0$	$P_1 = 0.1$	$M = 2.0$	$M = 3.0$
0.1	22	2.2	19.2	5.0
1.6	28	2.8	-	-

NOTE: ALL PRESSURES IN 10^5 Pa
1210-055W

Fig. 5-18 Test Nozzle Pressure Versus Time

100 ms. The maximum pressure in the test section, in the absence of a burst diaphragm or other pressure relief device during the course of a run, would be 34 and 3.4 MPa (336 and 33.6 atm) at P_1 equal to 100 and 10 kPa (1.0 and 0.1 atm), respectively. Figure 5-19 shows the approximate pressure on the end wall versus time for the case of P_1 equal to 100 kPa (1.0 atm). This plot indicates that the pressure rises very steeply to 2.2 MPa (22 atm) in about 200 μs and then gradually increases to 2.8 MPa (28 atm) in about 1.6 ms.

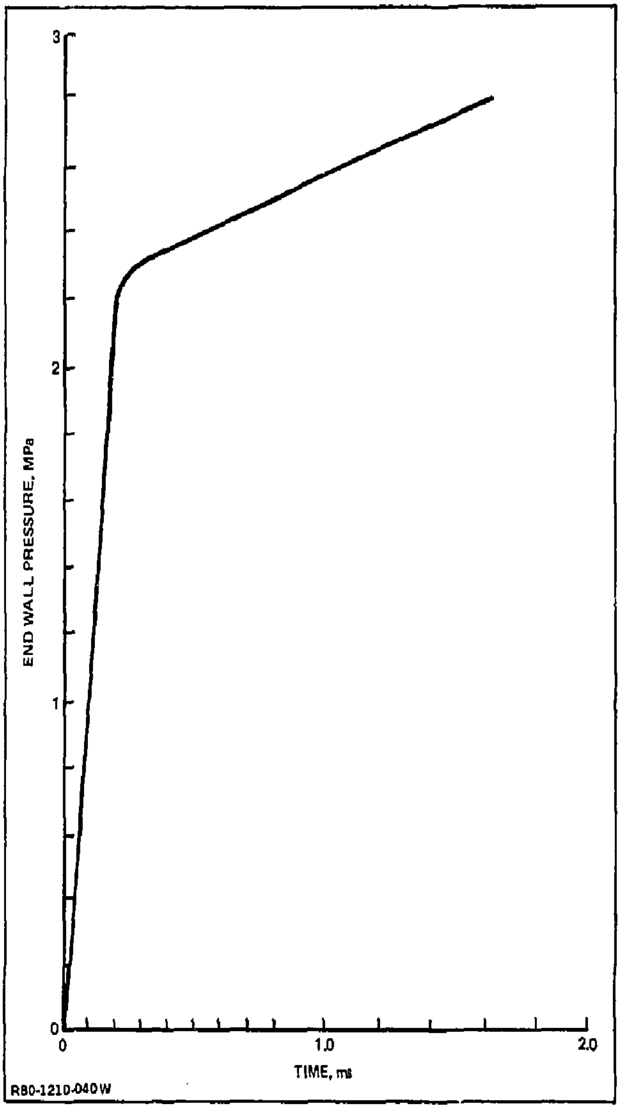

Fig. 5-19 End Wall Pressure Versus Time

Although Fig. 5-19 presents data for flow times up to 1.6 ms, the data of most interest occur in the first 200 μs. A gauge capable of taking the required data during this initial time period and also during the rest of the 1.6 ms is the Kulite Semiconductor miniature pressure transducer HKS-375-1000 (Fig. 5-20). With a filter to damp out the ringing, the gauge has a response time of 3 μs. Gauge repeatability is ±17.2 kPa (±2.5 psi). Provisions would be made to relieve the test nozzle pressure at 4 MPa (40 atm) to prevent overpressure destruction of the gauge which could occur at 10 MPa (100 atm).

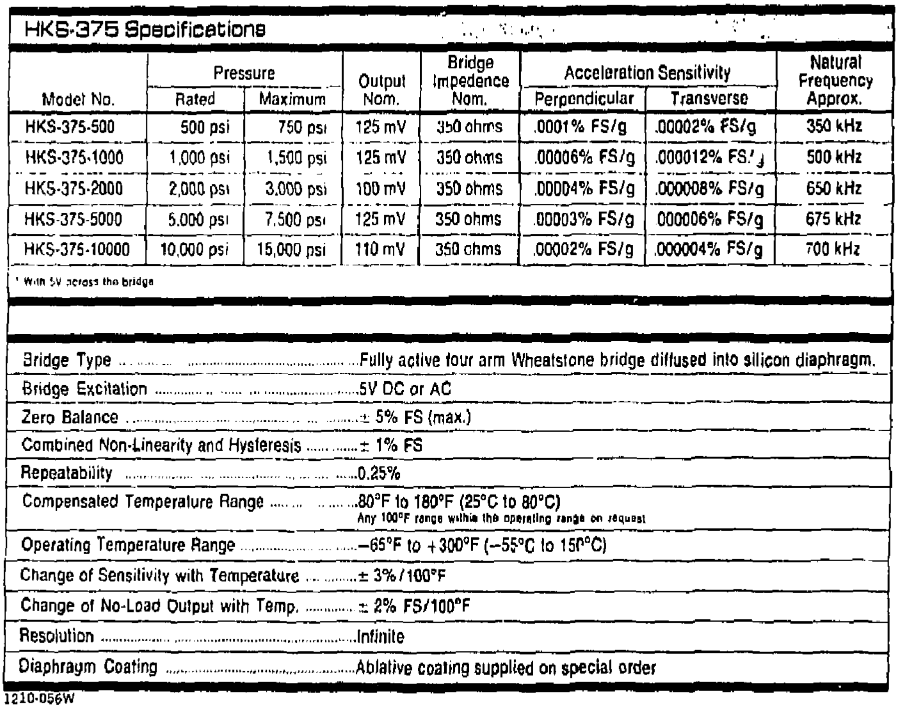

HKS-375 Specifications

Model No.	Pressure Rated	Pressure Maximum	Output Nom.	Bridge Impedence Nom.	Acceleration Sensitivity Perpendicular	Acceleration Sensitivity Transverse	Natural Frequency Approx.
HKS-375-500	500 psi	750 psi	125 mV	350 ohms	.0001% FS/g	.00002% FS/g	350 kHz
HKS-375-1000	1,000 psi	1,500 psi	125 mV	350 ohms	.00006% FS/g	.000012% FS/g	500 kHz
HKS-375-2000	2,000 psi	3,000 psi	100 mV	350 ohms	.00004% FS/g	.000008% FS/g	650 kHz
HKS-375-5000	5,000 psi	7,500 psi	125 mV	350 ohms	.00003% FS/g	.000006% FS/g	675 kHz
HKS-375-10000	10,000 psi	15,000 psi	110 mV	350 ohms	.00002% FS/g	.000004% FS/g	700 kHz

' With 5V across the bridge

Bridge Type	Fully active four arm Wheatstone bridge diffused into silicon diaphragm.
Bridge Excitation	5V DC or AC
Zero Balance	± 5% FS (max.)
Combined Non-Linearity and Hysteresis	± 1% FS
Repeatability	0.25%
Compensated Temperature Range	80°F to 180°F (25°C to 80°C) Any 100°F range within the operating range on request
Operating Temperature Range	−65°F to +300°F (−55°C to 150°C)
Change of Sensitivity with Temperature	± 3%/100°F
Change of No-Load Output with Temp.	± 2% FS/100°F
Resolution	Infinite
Diaphragm Coating	Ablative coating supplied on special order

1210-056W

Fig. 5-20 Pressure Gauge Specifications

5.6 LASER DOPPLER VELOCIMETER

5.6.1 System Description

Laser Doppler Velocimeter (LDV) systems determine velocity from a Doppler frequency shift in radiation that is scattered from an incident laser beam by the particles in a fluid flow.

For accurate measurements of local fluid velocity, the particles must be small and light enough to follow the flow, yet large enough to scatter a detectable signal.

This particle size requirement generally is not too restrictive for mean velocity measurements in a continuous flow, but it can be extremely restrictive for measurement of fluctuating velocity components in a turbulent flow, or for mean velocity measurements in a slightly unsteady flow.

A dual beam measurement system operating in a forward scattering mode is used, because for the chosen particle size range this mode yields the maximum scattered light signal. Aluminum oxide particles about 1 μm are used as the seed material. Aluminum oxide is selected because the refractory material withstands high gas temperature.

To obtain flow velocity measurements, two crossed laser beams are oriented so that the plane of the cross is parallel to the flow. The laser beam with a component in the upstream direction yields scattered light of higher frequency than the incident beam; the beam with a downstream component yields a lower frequency of scattered light. An optical detector focused on the crossing point of the two beams can detect the Doppler frequency difference between the light scattered by the two beams, which is a function of flow velocity, incident light frequency (λ), and the angle (θ_c) between incident beams and the velocity vector. The viewing angle of the receiving optics is unimportant, and is generally selected either for measurement convenience, or to obtain a maximum scattered light signal. The velocity is given by:

$$U = \frac{f_d(\lambda/2)}{\sin(\theta_c/2)} \qquad (5\text{-}10)$$

where f_d is the observed Doppler frequency. The Doppler frequency of a single particle passing through the interference fringes can be seen on an oscilloscope display superimposed on a broad low-frequency pulse caused by nonuniform light intensity in the incident beam.

Velocity determined directly from an oscilloscope signal display is impractical, not only because of accuracy limitations, but also because there are frequently several particles in the fringe pattern at any given time. An electronic signal processing system is used to collect Doppler signals which may be averaged for mean velocity measurements, and for evaluation of velocity fluctuations in turbulent or time-varying flows. Such processing systems include circuits to remove noise, electronic interference, and misleading signals that result from large particles or multiple scattering. Conservative adjustments of these circuits to obtain good data accuracy frequently results in the system rejecting far more signals than it accepts.

The short test times and high velocities in the Grumman Detonation Tube Simulation Facility mandated use of a counter system. A Thermo-Systems, Inc. (TSI) Model 1094 counter was selected because of its 100-MHz frequency measurement capabilities. This counter contains several circuits to reject noise and erroneous data that arise because the Doppler signal is discontinuous and of variable amplitude. Since experiment test times are so short, the controls for these circuits had to be preset at arbitrary levels, and fine tuning of the instrument could not be done in one run.

The counter consists of two discrete sections: the front end detector (FED) module and the logic and output display (LOD) module. The FED module has two circuits that can reject input data from the LOD module. One is a threshold setting to reject electronic noise. The required threshold level setting varies with particular measurement applications, but it is basically a function of the photomultiplier signal-to-noise ratio and the scattered light intensity level. Another discriminating circuit in the FED module is the overload (O/L) detector to reject signals which have excessive signal amplitude. Proper setting of the O/L detector will reject signals from extremely large particles (which could be moving much slower than the flow), or from a large number of particles passing simultaneously through the measurement volume.

The LOD module contains a logic circuit that rejects data which do not satisfy consistent frequency relationships. This circuit counts the time required for five Doppler cycles in the signal and compares it to the time required for eight Doppler cycles. If this time comparison is outside a given tolerance (variable by comparator setting), the data are rejected from display. This comparator circuit rejects erroneous data that could arise from several particles passing almost simultaneously through the periphery of the measurement volume.

The three data rejection controls described above (threshold level, O/L detector, and comparator setting) provide fine tuning of the processor to assure acceptance of valid measurement data. During conventional counter operation with a steady state flow, the operator can adjust all three settings in conjunction with the flow seed level to maximize the amount of good data accepted. For this experiment, it would be necessary to preset these controls, varying them individually from one run to the next to obtain more measurement points.

Flow seeding is accomplished by depositing a small amount of powder in the driven tube just upstream of the secondary diaphragm. The incident wave stirs up this powder before the secondary diaphragm ruptures and the reflected wave further mixes it into the shock-processed gas before it flows into the nozzle. All runs use Al_2O_3

powder nominally 1-μm diameter to obtain particles small enough to follow acceleration through the nozzle and to attain local flow velocity at the measurement section.

Driven tube gases, either shock heated or combustion heated, are expanded through a nozzle into the vacuum tank. Figure 5-21 shows a schematic of the test chamber LDV system setup used for velocity measurement close to the nozzle exit. The equipment components are shown in Fig. 5-22 and 5-23. The transmitting optics consist of a beam splitter, Bragg cell, and focusing lens. The scattered light detec-

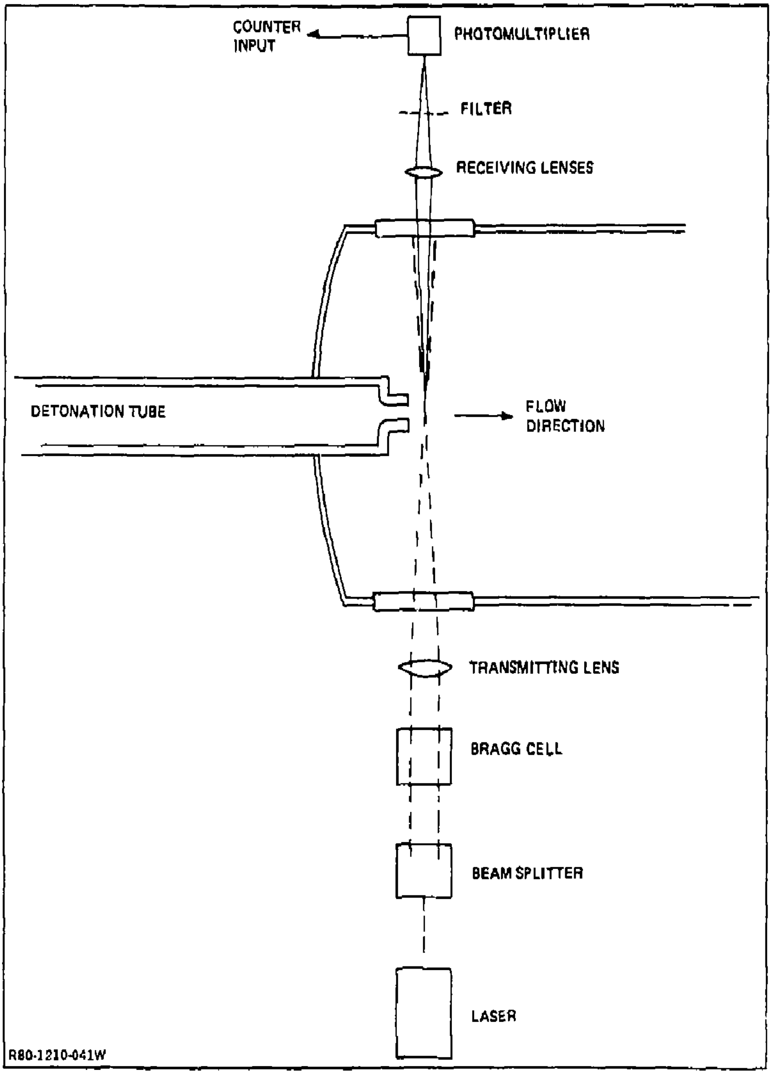

Fig. 5-21 LDV Measurement System Schematic

tion system consists of a collecting lens, a bandpass filter, a focusing lens, and a photomultiplier. The photomultiplier output feeds into the signal processor and its output is displayed on an oscilloscope.

A 1.2-m focal length lens in the transmitting optics brings the incident beam crossing point to the centerline of the vacuum tank. The incident beams before focusing *are spaced 22 mm apart to get the minimum angle of convergence* (ψ_c *in Eq 5-10)* so that the Doppler frequency would be as low as possible. Even with a small value of ψ_c, the high flow velocities for the combustion tests requires use of a Bragg cell to downshift the Doppler frequency so that it is measurable with the counter (less than 100 MHz).

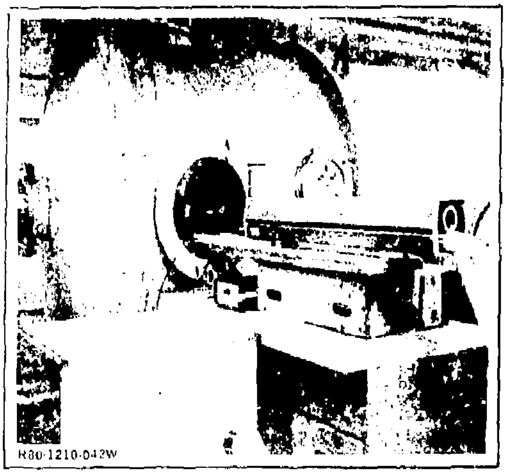

Fig. 5-22 Laser, Transmitting Optics, & Test Section

Fig. 5-23 Receiving Optics & Detector

5.6.2 Previous Test Programs

5.6.2.1 Experiments With a Combustion Heat Flow - An experiment was run in a combustion heat flow with the combustion gas running conditions shown in Fig. 5-24. The laser was a 2-W argon ion laser (Spectrophysics Model 164), transmitting only the green line at 5145 A. A Bragg cell was added to the transmitting beam optics to provide high frequency (and high velocity) measurement capabilities by shifting the frequency of one of the incident laser beams by 40 MHz with respect to the other. Because of the frequency difference between the two intersecting incident beams, the interference fringes appeared to be moving downstream. Thus, particles that were suspended motionless within the measurement region provided a scattered Doppler signal with an apparent upstream velocity corresponding to the 40-MHz difference in frequency between incident beams. Then particles moving downstream at 2000 m/s showed a scattered Doppler frequency of 33 MHz, rather than the 73 MHz that would have been obtained without the Bragg cell.

The gas stagnation properties for combustion runs are listed in Fig. 5-24. Stagnation conditions for the nozzle flow are denoted by variables with the subscript 5. The subscript 3 denotes expanded burned gas conditions at the exit plane of the two-dimensional nozzle used in these tests. The ideal values were calculated from the detonation wave speed associated with the fuel mixture in the driven tube, assuming a given incident shock velocity. The corresponding experimental values were based on the measured P_5/P_3 ratio during detonation tube operation. The ideal velocity represents the nozzle exit velocity as computed from the settling chamber conditions

PARAMETER	RUNNING CONDITIONS	
	IDEAL (FROM REF 5-3)	EXPERIMENTAL (BASED ON MEASURED P_5/P_3)
P_5, Pa	1.109×10^7	1.0688×10^7
H_5, cal/gm	578.4	578.4
T_5, K	3409	3406
P_3, Pa	8.18×10^5	7.033×10^5
T_3, K	2368	2323
M_3	2.311	2.371
γ_3	1.2051	1.2081
REYNOLDS NO.$_3$, m^{-1}	3.081×10^7	2.786×10^7
VELOCITY AT MEASURING LOCATION, m/s	2200	2203

1210-057W

Fig. 5-24 Combustion Gas Running Conditions Using Argon Ion Laser using a one-dimensional flow model, accounting for finite chemical reaction rates during the expansion. These test conditions have been used frequently for plume simulation work and supplementary data such as nozzle wall pressure measurements were consistent with the nozzle exit velocity.

Six runs were made at these test conditions for velocity measurements. In all these runs, the velocity measured during the 3-ms steady flow time was within a few percent of the predicted value of 2200 m/s. The averaged value of all measurements during the test time was 2203 m/s.

In four of these six runs, there was a delay between incident shock reflection (time of secondary diaphragm rupture) and fuel detonation, thus allowing unburned gas to flow through the measurement volume for a short period. From oscilloscope traces, the cold gas velocity was determined to be 1494 m/s, which compared favorably to subsequent calculations which predicted 1424 m/s. These additional data provided further confirmation of the value of LDV measurements in impulse-type flows. Also, the oscilloscope photos showed that useful data could be obtained after the steady flow time had ended, indicating that with refinement this system may be capable of time-resolving velocity measurements during the 3-ms flow of the combustion gases.

In these experiments, it was planned to obtain about 100 measurement points during a 3-ms run; however, only a few valid measurements were observed during any of the six runs. The measurement system was capable of providing far more data than this. The maximum signal data rate was determined by the counter, which can produce a new data point every microsecond. However, this maximum would be obtained only if one particle at a time crossed the measurement volume every microsecond, an unattainable situation in view of the random nature of the seeding process. The actual data rate was a function of both the particle seed distribution and the counter circuitry used to accept and validate data.

5.6.2.2 Particle Velocity Relaxation Experiment - An experiment was performed with a combustion heated flow to measure the particle velocity relaxation after passing through an oblique shock wave. The combustion gas running conditions are listed in Fig. 5-25. A shock wave was generated by a wedge mounted at the nozzle exit (Fig. 5-25). The flow Mach number upstream of the oblique shock was 1.78. Figure 5-26 shows mean velocity data obtained in the vicinity of an oblique shock with the LDV, as well as the theoretical velocity distribution and calculated velocity slip. The solid curve is the calculated particle velocity using 1-μm Al_2O_3 particles. The data and calculated particle velocity agree well, and the particles relax to within 3% of flow velocity in a slip length of 1.25 cm. This experiment pointed out an important experimental factor that must be considered when using an LDV for velocity measurements in flow patterns with velocity varying suddenly either in space or time; that is, there is a finite slip length or relaxation time for the particle to attain the flow velocity.

PARAMETER	RUNNING CONDITIONS	
	IDEAL (FROM REF 5-3)	EXPERIMENTAL (BASED ON MEASURED P_5/P_3)
P_5, Pa	8.086×10^6	8.136×10^6
H_5, cal/gm	278.0	278.0
T_5, K	2982.0	2982.0
P_3, Pa	1.881×10^6	1.730×10^6
T_3, K	2375.0	2343.0
M_3	1.657	1.706
$\gamma 3$	1.2122	1.2144
REYNOLDS NO.$_3$, m^{-1}	5.02×10^7	4.895×10^7
$\phi = 1.0, \alpha + \beta = 4°$, 1/20 SCALE 1210-058W		

Fig. 5-25 Combustion Gas Running Conditions Using LDV

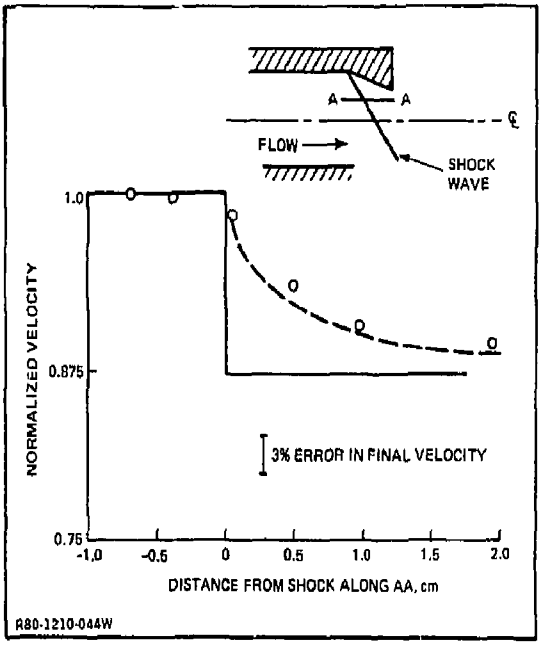

Fig. 5-26 Particle Velocity Relaxation After Oblique Shock

5.6.3 LDV Proof of Principle Experiment in Transient Flow

LDV velocity measurements are now made for particle slip lengths that are sufficiently long for the particles to attain free stream velocity. Furthermore, the test nozzle flow times are long enough to establish a usable particle flow at the velocity measurement station.

The proposed experiments will put very stringent requirements on the Grumman LDV measurement system. Because of the short time durations ($t \approx 200\mu s$) of interest, the velocity data rate must be maximized by controlling the particle number density. Such control has been accomplished for IR aerosol experiments by loading the driven tube with Al_2O_3 particles (Ref 5-3). This technique generates uniform, controlable aerosols, but with a small region near the shock tube end wall devoid of particles. As a consequence of this void, there is a time delay before particles arrive at the measuring station, in addition to the time delay caused by velocity slip.

To date, LDV operation has used micrometer size particles that are transparent to the 5145-A argon laser light. LDV data have always been taken in the forward scattering mode. However, the melting temperature of Al_2O_3 is approximately 3500 K which is less than the 5665 K temperature in Region 5 during the desirable driven tube test condition. It is unlikely that Al_2O_3 particles could be loaded into the driven tube for the T_S test condition of 5665 K, since small diameter particles equilibrate rapidly (Ref 5-3).

Other refractory particles can be used, but if the material is opaque, a switch would have to be made to a backward scattered system with a reduction in signal-to-noise ratio, or if the material is more dense, more velocity slip for the same particle size would result.

The seeding procedure must be done in such a manner that enough particles pass through the LDV light test volume to make measurements, but not so many at any one time that there is a high proportion of rejected data due to multiple particle light scattering. The ideal situation would be to have only one particle pass through the LDV light test volume every microsecond.

A particle injection mechanism, satisfying the three requirements necessary for good flow velocity data in a nominal 200-μs test time, must be demonstrated before the LDV technique can be adopted for velocity measurements in a blowthrough experiment. The three requirements for the injection mechanism are:

1. Initiation of particle flow into the test gas about 20 μs after start time

2. Adequate minimization of particle slip lengths or velocity relaxation times so that the particle velocity at the instrument test station is truly characteristic of the flow velocity
3. Adequate control of particle flow number density to satisfy the requirements that there be enough particles at the flow station to make a measurement, but not too many such that there would be an unreasonable fraction of rejected data.

An LDV proof of principle (POP) demonstration experiment could be run using an existing Grumman Shock Tunnel nozzle. The Mach number is 1.7 at the nozzle exit. Injection would be in the supersonic region of the test nozzle. This technique would satisfy Requirements 1 and 2, above. Various particle loading techniques would be tried to satisfy Requirement 3. Upon satisfactory demonstration that the LDV could be used to measure flow velocity in the test section within a 200-μs test time, the instrument would be utilized in the experimental program.

5.7 INFRARED EMISSION TEMPERATURE MEASUREMENT

5.7.1 Measurement Methods

The flow properties downstream of the nozzle exit will be monitored in the proposed tests using the IR emission bands of a suitable tracer gas seeded into the flow. Routinely, the 4.3-μm CO_2 fundamental is used for this purpose because of its large band strength and the availability of high temperature band model data. The plan is to use an eight-element indium antimonide IR detector to provide simultaneous radiance measurements along eight parallel lines of sight through the flow. The conversion of radiance values to temperatures will be performed using the measured wall pressures and the known temperature-pressure dependence of the IR emission bands:

$$I = \epsilon(\lambda, T, P)\, B(\lambda, T) \qquad (5\text{-}11)$$

where

I = radiant intensity

ϵ = tracer gas emissivity

λ = wavelength

T = temperature

P = pressure (measured by Kulite gauges)

B = Planck radiation function

The accuracy with which IR emission levels can be determined is limited to approximately 15% (giving approximately 10% temperature accuracy) as can be seen from the relation:

$$I \sim \text{const} \times P \times T^{3/2}$$

which is valid near anticipated experiment conditions and for a 4.3-μm wavelength. Relative temperatures along the various lines of sight will be determined more accurately. In all cases, the temperatures derived from IR emission pertain to weighted averages along the lines of sight.

5.7.2 Previous Test Programs

Infrared techniques have long been used to measure species temperatures and concentrations in shock tunnels. Two previous Grumman Research programs using IR techniques are briefly described below.

5.7.2.1 Scramjet Exhaust IR Measurements - The NASA Langley scramjet is an experimental engine designed to study and verify certain advanced hypersonic propulsion concepts (Ref 5-4). The current prototype installed in a 1.2-m (4-ft) diameter test tunnel burns hydrogen fuel in a hypersonic air stream for short (5 to 10 s) test intervals.

Exhaust gas temperature and water partial pressure are measured to determine the combustion efficiency of this engine. Because in-situ measurement of these quantities is difficult, Grumman investigated the applicability of nonintrusive remote sensing IR diagnostics to the scramjet facility. The specific approach is to monitor the IR emission of water vapor in the 2.7-μm ν_3 band. The spectral profile and absolute radiant intensity of this band are functions of water vapor temperature and partial pressure, and can be deduced from spectral data.

A rapid scan interferometer spectrometer is used to measure the scramjet spectra. The broad (2 to 5 μm) wavelength coverage of this instrument is important because it provides a means of distinguishing between true water vapor emission and that due to possible flow contaminants (NO_x, Cu, etc.) or thermal background. The excellent time-averaging capabilities of this instrument are similarly advantageous in the presence of signal fluctuations.

Diagnostic 2-to-5-μm IR spectra of the NASA Langley scramjet exhaust gases are measured with a rapid scan interferometer spectrometer at approximately 30-cm^{-1} (0.02-μm) resolution. System wavelength response is limited by the 2-μm cut-on of the germanium field lens and by the 5.4-μm cut-off of the indium-antimonide detector. Exhaust gases are viewed through a sapphire window along a line of sight perpendicular to the engine thrust line and 6 cm downstream of the exit plane (Fig. 5-27). To obtain mass averaged station radiation measurements, a cylindrical f/2 lens is used to produce a slit-shaped field of view that is 3.5-cm wide by 30-cm high (full width at half maximum). In-situ measurements with a point source IR blackbody indicate an overall 10% uniformity in response over the 24-cm span of the exit plane. The 25-cm atmospheric path length between the interferometer and the sapphire window is left unpurged, because atmospheric water vapor absorption over this small range is negligible. To check on the spatial uniformity of the exhaust gases, the field of view is reduced to a 2.5-cm-diameter circle. This permits spatially resolved measurements of spectra from the central, upper, and lower portions of the exit plane.

The observed mass averaged spectra are shown for various fuel equivalence ratios in Fig. 5-28. The fuel equivalence ratio (ϕ_i) is the relationship of the actual moles of molecular hydrogen in the fuel to that required for stoichiometric combustion of the hydrogen. These spectra exhibit the characteristic P, Q, and R branch structure of the ν_3 H_2O band with peaks near 2.9, 2.7, and 2.5 μm, respectively; and their intensity rises monotonically with increasing fuel equivalence ratio, ϕ_i. The IR intensity at low ϕ_i value (0.2, not shown) is too low for reliable background correction.

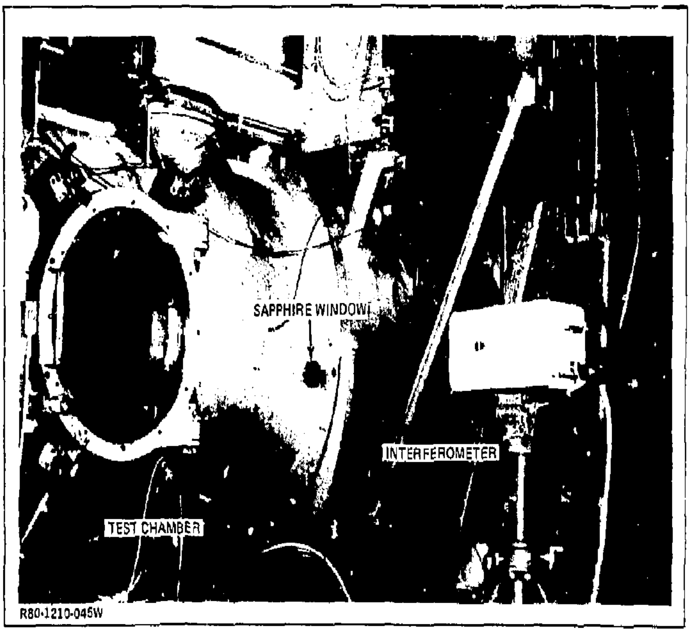

Fig. 5-27 Scramjet IR Emission Test Configuration

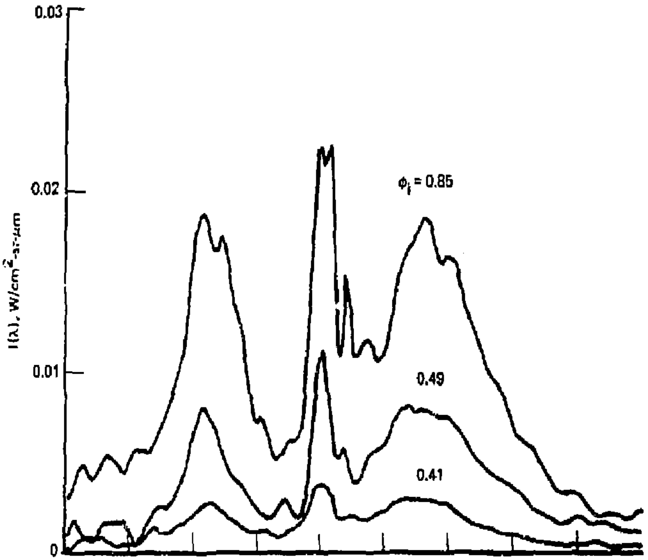

A. Measured exhaust H_2O vapor IR spectra showing monotonic increase with fuel equivalence ratio ϕ. Intensity maxima near 2.6, 2.7, and 2.9 μm correspond to *the R, Q, and P-branches, respectively, of the H_2O 2.7 μm ν_3 fundamental*

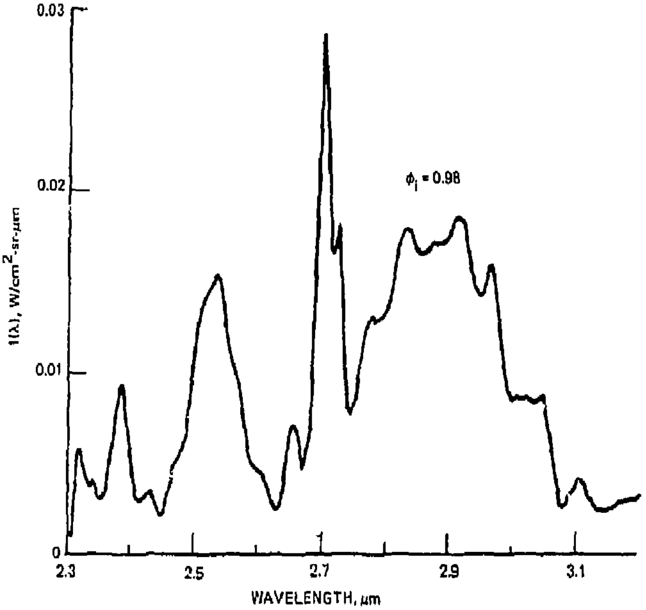

B. Spectrum measured for highest fuel equivalence ratio ϕ = 0.98. (Noise due to engine unstart and abrupt test run termination)

R80-1210-046W

Fig. 5-28 Scramjet IR Spectra

The spectrum for the highest ϕ_i value (0.98) represents the transform of a single interferometer and consequently is relatively noisy; the limitation to a single scan is due to engine unstart and test run termination. The remaining spectra are time averaged (2 to 4 s) results with fair scan-to-scan repeatability. The spectra show no evidence of interfering emission from hot metal parts, nitric oxides, or the zirconium oxide overcoating used on certain scramjet components. Figure 5-29 shows that the scramjet spectral profiles agree with the expected shape of the 2.7-μm water band, based upon Grumman radiation code calculations. This particular theoretical spectrum corresponds to a temperature of 1400 K and an H_2O pressure-path length product of 168 N/m, or roughly that expected for fuel equivalence ratio of 1 and a combustion efficiency of 50% (compare to Fig. 5-28B).

The subdivision of the 2.65-to-3.1-μm wavelength interval into two segments is made to facilitate spectral analysis of the temperature using the IR band ratio technique. This technique is analogous to two-color optical pyrometry, and is based upon the observation that the intensities of certain molecular emission bands are temperature sensitive. The results of the IR band ratio analysis are shown in Fig. 5-30.

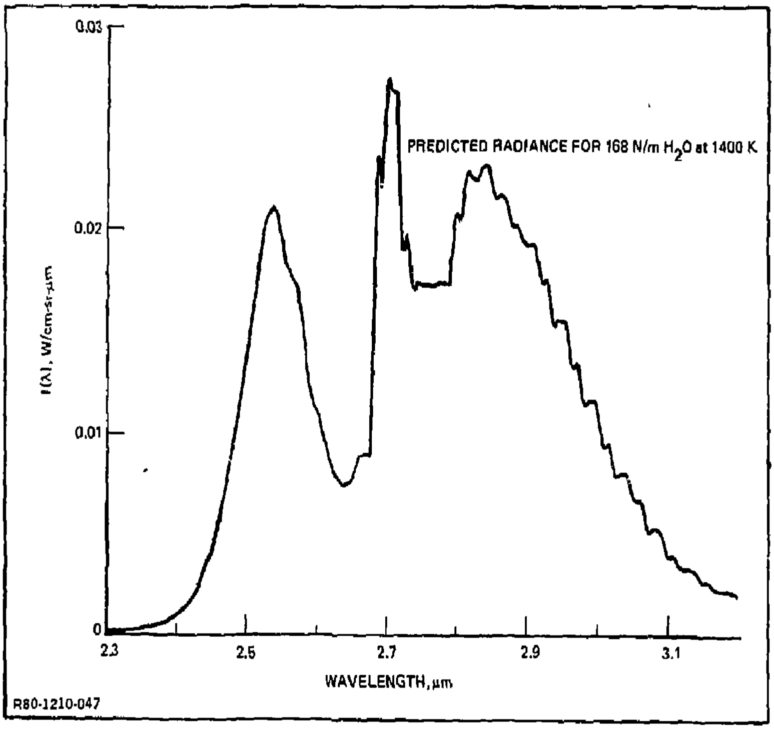

Fig. 5-29 Theoretical H_2O Spectrum

TEST PARAMETERS			MEASURED PARAMETERS	
RUN	ϕ_1	P_{static}, Pa	P_{H_2O}, Pa	T, K
165	0.41	8340	114	1500
164	0.49	8390	262	1600
166	0.85	7900	566	1625
164	0.98	8980	635	1625
1210-059W				

Fig. 5-30 Exhaust Gas Parameters Derived from IR Band Ratio Technique

5.7.2.2 IR Measurements of Sulfur Dioxide Decomposition Behind Shock Waves - Rate coefficients for the thermal decomposition of sulfur dioxide $SO_2 + M = SO + O + M$ have been measured (Ref 5-5). Sulfur dioxide-argon mixtures of 0.527, 0.26, and 0.13% behind reflected shock waves were heated in a conventional stainless steel shock tube. The IR emission from the band centered at 7.347 μm was monitored by a liquid nitrogen-cooled, mercury-cadmium-tellurium detector. The radiation was transmitted through barium-fluoride windows and isolated by an interference filter with a peak transmission wavelength of 7.362 μm, and half-power points at 7.256 and 7.469 μm. Data were taken using the three mixtures in argon noted above. At a given temperature, the IR emission is proportional to the sulfur dioxide concentration. Reflected shock temperatures were computed from the measured incident shock wave velocities, reactant mole fractions, and JANAF thermodynamic data. The temperature uncertainties were conservatively estimated as ±30 K at 3000 K.

Figure 5-31 shows a typical oscillogram of IR emission and of the output from a static pressure transducer. Both IR emission and pressure rise at the incident and reflected shock fronts. Data shown on the oscillogram cover a time interval of 350 μs from the initiation time of the reflected shock wave, thus indicating the utility of this technique in the microsecond flow processes. In this experiment very little dissociation of the sulfur dioxide took place at the pressure behind the incident shock wave. Therefore, the peak of the IR oscillograph reading is a measure of the SO_2 radiation before decomposition started to take place.

5.7.3 IR Temperature Proof of Principle Experiment in Transient Flow

In the proposed blowthrough experiment, multiple line-of-sight average temperatures will be taken and from these data a temperature profile at the test station will be constructed. Although single-channel data have been taken on an oscillograph in the characteristic time of 200 μs after initiation of a flow, it is desirable to have some multichannel IR data experience in a similar flow situation.

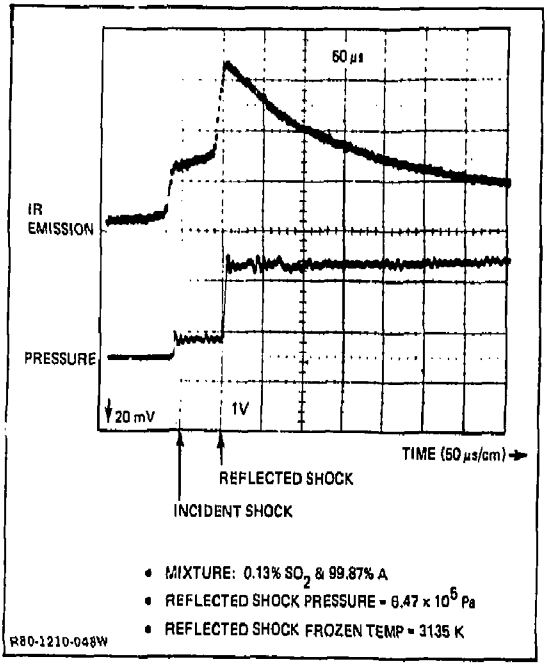

- MIXTURE: 0.13% SO_2 & 99.87% A
- REFLECTED SHOCK PRESSURE = 6.47×10^6 Pa
- REFLECTED SHOCK FROZEN TEMP = 3135 K

Fig. 5-31 Representative SO_2 IR Emission Oscillogram

An IR temperature measurement proof of principle demonstration experiment could be done at Grumman, with the optics and detector for the blowthrough experiment set up on an optical bench and absolutely calibrated with a blackbody source. Initially, low-temperature measurements will be taken with a gas cell. Then, the optical apparatus will be moved to the shock tunnel where high-temperature of a Region 5 gas and a starting flow will be measured. The starting flow tests will use an existing Grumman shock tunnel nozzle. The Mach number at the nozzle exit is 1.7 which will be close to the steady state Mach number at the test station of the blowthrough experiment nozzle.

5.8 TEST PROGRAM & SCHEDULE

Two options are available for the test program. In Option I, the stagnation pressure and temperature in Region 5 of the driven tube are used as the initial conditions for the code verification. The stagnation pressure and temperature are derived from the incident shock speed and stagnation pressure measurements. In Option II, the initial conditions for the code verification are obtained from measurements of velocity, pressure, and temperature at a test station located between the test section throat and the inner radius of the jet array.

Option I tests would be run at shock Mach numbers of 3.75 and 5.0, and at driven tube initial pressures of 10, 50, and 100 kPa (0.1, 0.5, and 1.0 atm) (as indicated in Fig. 5-12). The schedule shown in Fig. 5-32 shows a 27-week program. The 7-week test period includes 20 runs and provisions for one setup and a shake-down procedure.

The Option I test matrix of 20 tests is shown in Fig. 5-33. Tests will be conducted at Mach numbers of 3.75 and 5.0, at initial driven tube pressures of 10, 50, and 100 kPa (0.1, 0.5, and 1.0 atm). At all Mach numbers and pressures, tests will be conducted as calibrated runs without the array. Most tests will be run with the 13-mm (1/2-in.) diameter jet array. Some tests will have the 19-mm (3/4-in.) diameter jet array to determine the effects of jet diameter. Four tests will be duplicated to check the repeatability of the instrumentation; two without the array, and two with the 13-mm (1/2-in.) diameter jet array.

Under Option II, two proof of principle experiments would be run to determine the feasibility of using an LDV and IR emission measurements for velocity and gas temperature downstream of the throat of the test section. Five test runs with the LDV would be required to establish a velocity profile, with one separate test run to establish a temperature profile. The test section would be designed and built the same as in Option I. The schedule shown on Fig. 5-34 includes 4 and 6 weeks for the LDV and IR temperature proof of principle experiments, respectively. These experiments would be completed in the first 8 weeks of the test schedule. The Option II test schedule runs for 33 weeks. The 13-week test period includes 50 runs and provisions for one setup and a shake-down procedure.

5.9 CONCLUSION

A shock tunnel experiment has been designed to experimentally verify a one-dimensional computer code describing the flow of a lithium plasma over a jet array. Complete experimental verification of the code is desirable, but the generation of the high temperatures and energies involved, plus the use of liquid lithium, makes such an experiment complex, time consuming, and expensive. However, a major portion of the code can be simply verified experimentally in the regime of low energy flow over simulated jets, where little disturbance is imparted to the jets in the form of radiative transfer, erosion, or vaporization.

The test section consists of a 30-deg sector of a right circular cylinder, 25-mm (1-in.) thick. It attaches to the end of the shock tunnel driven tube. The jet array

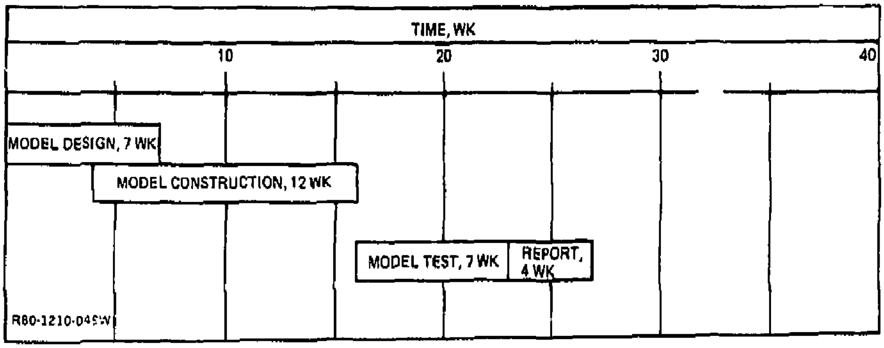

Fig. 5-32 Option I Test Schedule

MACH NO.	3.75	3.75	3.75	5.0	5.0	5.0
PRESS., 10^5 Pa	0.1	0.5	1.0	0.1	0.5	1.0
NUMBER OF RUNS						
WITHOUT ARRAY	1	1	2	1	2	1
1.27 cm JETS	1	1	2	1	1	2
1.905 cm JETS	1	–	1	–	1	1

R80-1210-051W

Fig. 5-33 Option I Test Matrix

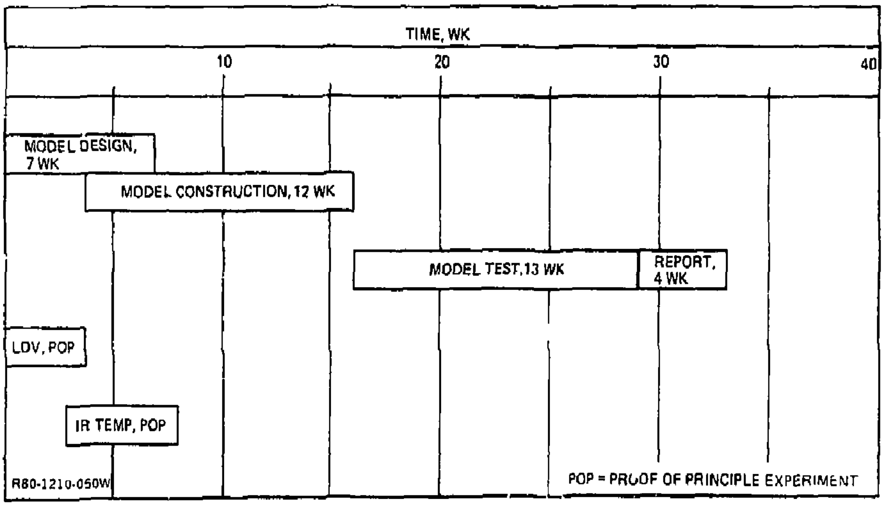

Fig. 5-34 Option II Test Schedule

is represented by rigid cylindrical posts fastened to the test section in a pattern that will simulate the one-dimension area function used in a previous computer run.

A major purpose of the test program is to measure the time varying fluid pressure in the test section. Measurements will be made with and without the jet array present.

A test program with two options is presented. In Option I, the pressure and temperature in the stagnation region of the driven tube are used as test initial conditions. Separate experimental runs are proposed to determine the temperature and velocity profiles. In Option II, the initial conditions of pressure, temperature, and velocity are experimentally determined at a test station downstream of the test section throat. Pressures are measured with pressure transducers.

Proof of principle experiments for determining the velocity by laser Doppler velocimeter and the temperature by IR emission are recommended and described.

5.10 REFERENCES

The following references have been cited in this section:

5-1 Lawrence Livermore National Laboratory, "Divergent Impulsive Crossflow Over Packed Columnar Arrays," by L.A. Glenn, Preprint UCRL-83051, July 1979

5-2 Von Mises, R., Mathematical Theory of Compressible Fluid Flow, Academic Press, 1958, p. 73

5-3 Grumman Aerospace Corporation, "A Technique for Controlled Gas/Particle Experiments," by R.A. Oman, W. Konopka, and V.S. Calia, RM-686J, April 1979; also, Proceedings of 2nd Multiphase Flow and Heat Transfer Workshop, Miami, Fla., April 1979

5-4 National Aeronautics and Space Administration, "Infrared Measurements of a Scramjet Exhaust," by R. Reed and M. Slack, CR-3242, January 1980

5-5 Grillo, A., Reed, R., and Slack, M., "Infrared Measurement of Sulfur Dioxide Thermal Decomposition Rate in Shock Waves," Journal of Chemical Physics

6 - ENGINEERING TEST FACILITY PLANNING

6.1 INTRODUCTION

The Engineering Test Facility (ETF) is a proposed testbed for Inertial Confinement Fusion (ICF) reactor engineering and technology. This study was performed to provide a preliminary assessment of ETF objectives and expected results, and although it used the HYLIFE ICF concept as a model, the program thus defined could be adapted readily to other ICF driver/energy converter methods. Energy converter development, which has not been pursued vigorously, would have particular benefit from an ETF program.

The practical consideration of ICF as a commercial energy source requires significant development activities in three areas:

- Driver
- Pellet target
- Energy converter.

Driver development and target physics are being explored intensively both theoretically and experimentally, in ongoing ICF programs at LLNL, LANSL, Sandia, and other facilities. However, engineering considerations of a device to convert to useful form the pulsed fusion energy, which is the ultimate goal of the ICF physics program, are being addressed only on a small scale. The energy converter comprises the reaction chamber which includes a first wall and blanket, a tritium breeder, and a system for transferring the fusion energy to the electrical power system. Experience with development of other new technologies indicates that engineering development time will be substantial for ICF energy converters.

Engineering development of an ICF energy converter necessarily would be a phased development that could progress within the following ICF program:

- Phase I - Engineering Test Facility to provide a focus for developing and testing reactor-relevant technologies and components

- Phase II - Experimental Power Reactor that would operate in a continuous duty cycle and produce power
- Phase III - Full-scale Demonstration Power Reactor that would produce reliable, but not necessarily, economical power
- Phase IV - First Commercial Plant.

The study outlined the current state of planning for an ICF ETF, and the engineering development that must precede it. The preconceptual design of the laser-driven HYLIFE reactor concept was used as a guide in developing this ETF plan. However, the plan could be applied easily to any of the ICF driver/energy converter concepts.

This ETF plan assumes that the ICF ETF will use the first driver-target facility to produce fusion energy power of over 10 MW at a reasonable repetition rate. It appears that the proposed Single Pulse Test Facility (SPTF) could be upgraded to have repetition rate capability. If either a laser or a heavy ion beam is chosen as the SPTF driver, a dual ETF/target-physics facility may be feasible.

The current study developed a set of objectives and anticipated results for the ETF, and provided a time-phased scenario of typical events. It identified technology issues that should be resolved prior to ETF operation.

6.2 OBJECTIVES FOR FIRST ICF ETF

The ICF ETF will be the first ICF facility to mate reactor components with the driver-target combination developed by the ICF physics program. As such, it will demonstrate the capability to integrate successfully the three major ICF subsystems (driver, target, and energy converter). Since these three subsystems are only loosely coupled in a final system, technology development will continue to proceed relatively independent in each area until final integration in ETF.

The ETF will not generate electricity from its steam loop, because that procedure is standard and would be uneconomic at the anticipated power level and duty cycle.

The ETF will be followed by an Experimental Power Reactor (EPR) with a continuous duty cycle and approximately 50% availability. This EPR will be followed by a full-scale demonstration power reactor that will generate reliable electricity.

The objectives for ETF are:

- Provide a data and technology base useful in the design of both the experimental power reactor and the demonstration power reactor.
- Use the first "rep-rate" capable, multimegajoule driver constructed for the ICF target physics program to demonstrate the integrated operation of reactor subsystems at significant fusion power levels (10 to 100 MW).
- Retain the flexibility to select the driver and converter concepts relatively late in the design schedule
- Have the capability of up to 1000 consecutive shots at a pulse rate of 0.1 to 10 shots per second, once per day, 100 days per year, for 5 years
- Integrate the following systems to operate on-line at the design pulse rate:
    - Pulsed power conditioning system for the driver
    - Driver
    - Final beam handling device
    - Target injection and tracking system and driver trigger system
    - Target (compression and thermonuclear burn)
    - Reaction chamber
    - Reaction chamber diagnostic systems
    - Vacuum pumping
    - Liquid metal circulation
    - Tritium breeding system
    - Primary to secondary to water loop heat transfer systems
- Integrate the following systems to operate off-line as required:
    - Target fabrication (up to 200 targets per day)
    - Impurity and hydrogen isotope removal from the primary, secondary, and water loops
    - Tritium reprocessing

  - Remote maintenance of the reaction chamber and internal diagnostics
  - Liquid metal component cleaning and handling facility

- Have the capability to expose material samples to the fusion pulses at radii much smaller than the wall radius
- Have the capability to be upgraded (following completion of the ETF experimental program) to a material test or tritium production facility that can operate continuously at the design rep-rate with 50% availability.

6.3 ASSUMED ICF KNOWLEDGE PRIOR TO ETF OPERATION

Significant technological advances will be required between now and the final design, construction, and operation of the ICF ETF. Development plans including cost and schedule projections will be required for each of the major technology areas. Some technology issues will require full-scale experimental verification prior to design commitment, while other engineering decisions may be made based on calculations only. In this subsection, an effort has been made to list all of the major ETF technology issues, by subsystem, and to project the levels of engineering certification/verification required as a minimum, prior to ETF operations.

The suggested levels of certification and their code letters (A through F) used in the subsystem listings are defined below:

A = Tested in an experiment with a full-scale module

B = Tested in a scale-down experiment

C = Tested in the initial stage of SPTF

D = Tested in the shakedown of ETF (prior to fusion pulses)

E = Tested on similar facilities for a different fluid

F = Calculated only.

The technology issues and levels of certification by subsystems are:

- *Pulsed power conditioning:*
  - *Provide conversion of steady power to pulsed power* (A)
  - *Have a lifetime of* 10^5 pulses (A)
  - Have variable rep-rate 10^5 capability (A)

- Driver:
  - Provide appropriate energy and power (measured just before entering the final beam handling device) (B, C)
  - Have variable rep-rate capability (0.1 to 10 Hz) (B)
  - Have appropriate beam quality (measured just before entering the final beam handling device) (B, C)
- Final beam handling device:
  - Be protected from the effects of X-rays and pellet debris (B)
  - Have a reasonable lifetime under neutron irradiation (with acceptable beam quality just after exiting this device) (B)
  - Number and clustering of devices is reasonable (F)
  - Can operate when coupled to a vibrating system (B)
- Target injection and tracking system and driver trigger system:
  - Target survival of injection and heating in chamber (experiment may simulate chamber environment) (A)
  - Target can be tracked and trajectory predicted (A)
  - Driver can be triggered at the appropriate instant (B)
  - System can survive effects of fusion pulse including impact of hot liquid or vapor from a fluid first wall (F)
  - System will not provide a leakage pathway for liquid metal or tritium (F)
  - Can operate when coupled to a vibrating system (A)
- Target (compression and thermonuclear burn):
  - Gain of 5 to 50 with driver energy of 2 to 5 MJ demonstrated (C)
  - Gain attainable with injected target (F)
  - Time resolved neutron, X-ray, and debris spectra known (B, C)
- Reaction chamber:
  - Material properties and equations of state known (B)
  - Upper bound response to fusion known (E, F)

  - Time to reestablish chamber conditions known (E, F)
  - Fluid wall establishment when nozzle is vibrating is assured (if fluid wall is the reactor concept selected) (B, D, E)
  - Beam quality not catastrophically degraded by chamber interior (E)
  - Target injection and tracking not catastrophically degraded by chamber interior (E)
- Reaction chamber diagnostic systems:
  - Measure wall position, temperature, and strain versus time (B)
  - *Measure fluid wall reaction to fusion pulse* (E)
  - Measure vapor composition, temperature, pressure, and density as a fu tion of location and time (E)
  - Measure vibration frequencies and amplitudes of key components (B)
  - Measure target output spectra versus time (B, C)
  - Measure tritium concentrations in fluids (B)
- Vacuum pumping:
  - Reestablish initial chamber pressure with appropriate mass flow and delta-P conditions (B)
  - Clear impurities from pump system (B)
  - Withstand or be protected from hot liquid and vapor (B, E)
- Liquid metal circulation:
  - Develop appropriate head and flow rate (B, E)
  - Operate with impurities in the liquid metal (B, E)
  - Withstand or be protected from pressure surges in the fluid (A)
  - Be sufficiently reliable to prevent liquid metal spills and have backup safety systems to cope with a spill (B, E)
- Tritium breeding system (all the hardware for this system is included in other systems)

- Primary to secondary to water loop heat transfer systems:
  - Transfer heat according to specifications (B, D)
  - Be sufficiently reliable to prevent liquid metal spills and have backup safety systems to cope with a spill (B, E)
- Target fabrication:
  - Produce 300 targets of acceptable quality per day (B)
- Impurity and hydrogen isotope removal from primary, secondary, and water loops:
  - Can be done off-line in a batch process (B, E)
  - Can recover and separate hydrogen isotopes from other impurities and separate protium from H, D, T. (B, E)
- Remote maintenance of reactor chamber and internal diagnostics:
  - Visually inspect chamber between shots (B, E)
  - Remotely disassemble chamber components (B, E)
- Liquid metal component cleaning and handling facility:
  - Facility performs to specifications (B, E).

6.4 ANTICIPATED ETF ACHIEVEMENTS & MILESTONES

The ETF will prove the capabilities of its subsystems to operate as designed, both in isolation and within an integrated facility that performs virtually all of the functions of a power reactor on a small scale.

The ETF also will demonstrate the lifetime of some of its key components.

The ETF will determine the degree of conservatism in the calculations of the system response to fusion, and enable design of future facilities that will be more compact and economical.

The ETF will uncover unanticipated technology and engineering problems that need to be solved prior to commercialization of ICF technology.

Finally, the ETF will provide the basis of a facility that can be used to conduct long-term materials studies in a pulsed radiation environment with appropriate stresses and corrosion influences on the material samples.

Specific milestones for three types of experiments are:

- Single-shot experiments:
  - Determine the response of the wall (fluid and/or structural) to the fusion pulse
  - Provide an estimate of the chamber reestablishment time
- Two-shot experiments:
  - Demonstrate reestablishment of initial conditions
  - Demonstrate target injection/tracking and beam propagation in the nonquiescent environment
- Thousand-shot experiments:
  - Demonstrate operation under steady-state conditions (complete establishment of thermal, vibrational, and noncondensible gas conditions)
  - Measure degradation of material properties under liquid metal corrosion, cyclic stress, and pulsed radiation (limited experiments are possible; long-life experiments need a material test facility)
  - Verify tritium breeding ratio and system multiplication factor calculations.

6.5 TYPICAL ETF OPERATIONAL SCENARIO

A typical ETF operation scenario is shown in Fig. 6-1. The scenario begins with a pretest phase where initial driver assembly and checkout is performed as part of physics-target facility activation. ETF operations begin as the driver is upgraded to multiple shot capability. ETF baseline operations would typically include a 1000-shot sequence at the 1-Hz rate. A 1000-shot sequence would nominally occur once a week, and would include the following sequence of events:

- Preheat liquid metal to startup temperature
- Start flow
- Inject and track dummy targets and align driver
- Inject and drive up to 1000 targets at the design rep-rate while reading data
- Divert liquid metal to insulated dump tank
- Stop liquid metal circulation systems

- Reduce data.
- Remotely service chamber diagnostics and perform any necessary maintenance.

It is expected that most of the engineering development testing could be completed over a 5-yr period. The ICF ETF could then be reconfigured either as a Material Test Facility (MTF) or as a tritium production facility, depending on the programmatic needs.

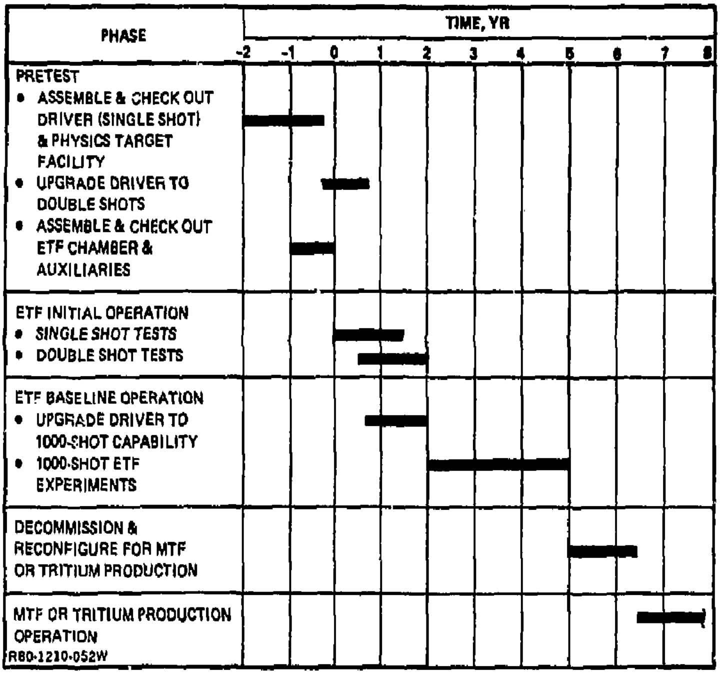

Fig. 6-1 Typical ETF Operational Schedule